Fingerprints of collisionless reconnection at the separator, I, Ambipolar-Hall signatures

J. D. Scudder,[1] F. S. Mozer,[2] N. C. Maynard,[3] and C. T. Russell[4]

Received 3 May 2001; revised 16 January 2002; accepted 16 January 2002; published 15 October 2002.

[1] Plasma, electric, and magnetic field data on the Polar spacecraft have been analyzed for the 29 May 1996 magnetopause traversal searching for evidence of in situ reconnection and traversal of the separator. In this paper we confine our analysis to model-free observations and intrasensor coherence of detection of the environs of the separator. (1) We illustrate the first documented penetration of the separator of collisionless magnetic reconnection in temporal proximity to successful Walén tests with opposite slopes. (2) We present the first direct measurements of $E_{\|}$ at the magnetopause. (3) We make the first empirical argument that $E_{\|}$ derives from the electron pressure gradient force. (4) We document the first detection of the electron pressure ridge astride the magnetic depression that extends from the separator. (5) We provide the first empirical detection of the reconnection rate at the magnetopause with the locally sub-Alfvénic ion inflow, $M_i^A \simeq 0.1$, and trans-Alfvénic exhaust at high electron pressure of $M_i^A \simeq 1.1-5$. (6) We exhibit the first empirical detection of supra-Alfvénic electron flows parallel to **B** in excess of 5 in narrow sheets. (7) We illustrate the detection of heat flux sheets indicative of separatrices near, but not always in superposition, with the supra-Alfvénic parallel electron bulk flows. (8) We present the first evidence that pressure gradient scales are short enough to explain the electron fluid's measured cross-field drifts not explained by $\mathbf{E} \times \mathbf{B}$ drift but predicted by the measured size of $E_{\|}$. (9) We illustrate that the size of the observed $E_{\|}$ is well organized with the limit implied by Vasyliunas's analysis of the generalized Ohm's law of scale length $\rho_s = \beta^{\frac{1}{2}} \frac{c}{\omega_{pi}}$, indicative of the intermediate scale of the diffusion region. (10) We document the first detection of departure from electron gyrotropy not only at the separator crossing but also in its vicinity, an effect presaged by *Vasyliunas* [1975]. (11) We make the first reports of very large values of electron $\beta_e \simeq 680$ localized at the separator, which imply that the electron thermal gyroradius exceeds the electron inertial length by more than an order of magnitude there. This clearly delineates that the environs of the reversed field region in this data contain non-MHD scales. The ambipolar association and the measured $E_{\|}$ data imply the presence of the nonideal ρ_s scale in these layers surrounding the null point. The high β_e signals the possible demagnetization of the thermal electrons in any structures with spatial scales of the electron skin depth, which is theoretically anticipated to surround the magnetic null line of the separator proper. This possibility is supported by the large number of temporally unaliased spectra at high β_e that are inconsistent with gyrotropy. *INDEX TERMS:* 7835 Space Plasma Physics: Magnetic reconnection; 2724 Magnetospheric Physics: Magnetopause, cusp, and boundary layers; 7815 Space Plasma Physics: Electrostatic structures; 2712 Magnetospheric Physics: Electric fields (2411); *KEYWORDS:* scales, separator, magnetic reconnection, parallel electric fields, magnetopause, cusp

Citation: Scudder, J. D., F. S. Mozer, N. C. Maynard, and C. T. Russell, Fingerprints of collisionless reconnection at the separator, I, Ambipolar-Hall signatures, *J. Geophys. Res.*, *107*(A10), 1294, doi:10.1029/2001JA000126, 2002.

[1]Department of Physics and Astronomy, University of Iowa, Iowa City, Iowa, USA.
[2]Space Sciences Laboratory, University of California, Berkeley, Berkeley, California, USA.
[3]Mission Research Corporation, Nashua, New Hampshire, USA.
[4]Institute of Geophysics and Planetary Physics, University of California, Los Angeles, Los Angeles, California, USA.

0148-0227/02/2001JA000126$09.00

1. Introduction

[2] Interpretations are frequently found in the literature that link in situ measurements with posited collisionless magnetic reconnection removed from the sites of data collection (e.g., for reviews, [*Cowley*, 1980; *Onsager and Lockwood*, 1997; *Paschmann*, 1997]). Many theoretical recipes exist for sustaining collisionless magnetic reconnection. Frustratingly, there have been virtually no observatio-

nal constraints placed on the mechanisms by which these recipes differ. With this series of papers we alter this situation by presenting analyses from a suite of measurements performed by the GGS-Polar spacecraft as it penetrated on 29 May 1996 the singular separator line of magnetic reconnection theory.

[3] The purposes of the present paper are to show that short (non-MHD) scales are present in this layer, to establish the measurements for $E_{||}$, to show that these observations were in regions near a virtual null point in the magnetic field which contain Alfvén waves that pass the Walén test (using electrons) with opposite slopes, to illustrate a pressure ridge of electrons along the current-carrying layer, highlighting regions of flow that are sub-Alfvénic and supra-Alfvénic, and to present parallel supra-Alfvénic electron flows in regions where previous Walén tests had been certified. All of these properties have a coordinate-free character but are predicted by the most modern pictures of the reconnection layer in the collisionless limit. These associations involve observables that are one step removed from engineering data yet are free of ad hoc coordinate system choices.

[4] Many specific predictions of reconnection dynamics involve components of this or that vector or tensor along special directions of the geometry of the process. When a spacecraft skims along the boundary, spending a long time in its vicinity, the geometry is not simply determined by the time series of the data along the orbit of the spacecraft but must be constructed assuming self consistency of the data, since the orientation and velocity of the ''natural'' coordinate systems for picturing the process are not known in advance. We have found such a natural coordinate system, and in the sequel to this paper we will discuss the data in that coordinate system. However, the leverage to find that system is the integrity of the basic measurements. In this paper we establish the basic integrity of the measurements including several new ones while relating them to the reconnection signatures noted above.

[5] In the ideal MHD description the separator of magnetic reconnection is a one-dimensional curve of zero thickness and nonzero length; in resistive MHD the ''diffusion'' region about the separator has one scale length controlled by the resistivity assumed. In many cartoons of reconnection, this scale is the size of the ''black box'' region around the intersection of the separatrices. In the collisionless nonideal MHD theory, the separator's vicinity is composed of three nested layers with generally distinct spatial scales: an inner region with the electron inertial length, $d_e \equiv \frac{c}{\omega_{pe}}$, as its typical scale; an intermediate region with typical acoustic length scale length, $\rho_s \equiv \beta^{\frac{1}{2}} \frac{c}{\omega_{pi}}$; and an outer region with spatial scales of the order of the ion inertial length, $d_i \equiv \frac{c}{\omega_{pi}}$. Here ω_{pj} is the plasma frequency associated with the j'th species. On the d_i scale, electron and ion fluids follow different paths enabling current flow; electrons follow $\mathbf{E} \times \mathbf{B}$ paths, while ions do not, and the ions are partially, if not totally, unmagnetized. On the ρ_s scale, electrons are seen to have perceptible pressure gradient drifts in addition to electric drifts, but the electrons remain magnetized. On the inner d_e scale, especially near nulls with weak B, the electron $\beta_e \gg 1$ so that the thermal electrons become unmagnetized and their velocity distribution functions may become noticeably nongyrotropic. In the collisionless picture of reconnection summarized by *Vasyliunas* [1975], the process cannot become steady without such nongyrotropic electron distributions in the immediate region that includes the separator line. We will refer to the separator and its environs to include these three spatial layers; conversely, the complementary space outside these layers contains the MHD external flows where rotational discontinuities (RDs) and slow shocks will be found. We offer this definition of ''detection'' that involves all three separate scales of the nonideal separator regime as more robust than the $\frac{c}{\omega_{pi}}$ scale arguments put forward by *Oieroset et al.* [2001].

[6] Outside of these environs of the ''black box'' of the diffusion region are the MHD structures associated with RDs and possibly slow shocks embedded in the external flow; these afford a larger scale matching between the inflowing material and the outflowing matter necessitated by the physics at the separator and the boundary conditions that resupply flux to the region. Until now all empirical evidence presented in the literature associated with reconnection has pertained to signatures in this external region. In this sense traversing the magnetopause away from the separator permits RD and slow shock diagnoses to be inverted to infer reconnection along separator lines not traversed. Such traversals will, in general, possess at least the d_i scale for the Chapman Ferraro currents to be supported and will, in general, have some **B** magnitude variation that attends the rotation of the field (as appropriate for a rotational discontinuity in the presence of pressure anisotropy). Thus depressions in **B** at the magnetopause by themselves only directly comment on the presence of the d_i scale in the layer. It is the incidence of the further narrowing of the current channels outlined above that differentiates the ''open magnetopause away from the separator'' from the ''open magnetopause at the separator.'' Thus penetration of the diffusion region, in the above collisionless sense, would require detections of signatures associated with all three of these scales. In the zero-guide field limit the innermost scale is by definition that about the null in **B**. Detection of the inertial length scale in the finite guide field limit requires a scale length determination.

[7] Thus the key to recognizing the diffusion region, per se, is the ability to detect spatial scales of structures found in time traces of derived parameters. This is an old problem. There are new approaches to the issue of inferring scales. One of the most exciting techniques is the comparison of an observable related by theory to the gradient of another observable. Such an example is the direct detection of a current density related by Maxwell's equations to the curl of the **B** field. If a DC **J** is measured, order of magnitude scales of the spatial variation of **B** are available. Similarly, if ambipolar contributions to **E**, such as its component along the local magnetic field, $E_{||} \equiv \mathbf{E} \cdot \hat{\mathbf{B}}$, and the electron pressure are simultaneously observed, there is information about the requisite scale lengths that must be present in the pressure profile. We will use the newly available $E_{||}$ measurements to infer the presence of the ρ_s scales of the intermediate region of the diffusion zone. We will present evidence that the observed β_e becomes so large that the electron thermal gyroradius becomes much larger than the d_e minimum scale length thought to be relevant at the null point. The β_e variation maximizes in the weakest field

regimes. Measures of nonidealness are required for the process of magnetic reconnection to be realizable. As important as the $\mathbf{J} \times \mathbf{B}$ Hall physics is near the separator [*Vasyliunas*, 1975; *Sonnerup*, 1979; *Shay et al.*, 2001], it is not a nonideal feature of MHD. Restating this important result, retention of the Hall term merely requires that when there is a cross-field current present, the cross-field center of mass motion of the plasma does not "carry" the magnetic field; rather, the cross-field electron motion does so in the absence of scales in the plasma below d_i. In fact, the retention of the $\mathbf{J} \times \mathbf{B}$ force as a correction to the unipolar proxy electric field, $-\mathbf{U}_{com} \times \mathbf{B}$, is at best an approximation to saying that the electrons carry the magnetic field, a result that follows exactly from the electron momentum equation [*Rossi and Olbert*, 1970]. Accordingly, the Hall physics cannot by itself contribute to the initiation of reconnection, even though it may have an important impact on the sustainable rate of reconnection permitted by other "agents."

[8] Post-Hall physics contributions to $\mathbf{E}$ with nonzero curls are required to sustain reconnection. These terms in their usual order of importance are the "ambipolar electric field," $E_{ambi} = -\frac{\nabla \cdot P_e}{en_e}$, the electron inertial contribution $E_{\text{inertial}} = -\frac{1}{en_e}\frac{D}{Dt} m_e n_e \mathbf{U}_e$, and the resistive or collisional drag resistive emf usually modeled as $E_{\text{resistive}} = \eta \cdot \mathbf{J}$. The advective derivative has been used in the definition above of the inertial term. The resistivity, η, is proportional to the ion electron drag and is proportional to the electron mass, so it is formally of the same order as the inertial term. In a collisionless plasma, η depends on the spectral power density of waves that can induce the scattering of electrons. There is generally no a priori reason that the drag emf should have this frequently assumed form, borrowed from high-density collisional plasmas. However, the main distinction between these post-MHD terms is that E_{ambi} does not depend on the electron's inertia and is usually larger than the other terms by a substantial margin unless the electrons are postulated to have zero temperature [*Scudder*, 1997]. Binary collision frequencies are such that resistive effects play no role in reconnection near the earth or interplanetary medium.

[9] At the simplest level in MHD, magnetic tubes of force are often envisaged as if they were electrical equipotentials. The occurrence of electric fields along the local magnetic field, $E_{\|}$, vacates this mental construct. In the magnetospheric context it was foreseen [*Stern*, 1973; *Greene*, 1988] that different field lines emerging from neutral points at each cusp must have distributed electrical potentials on them, so that the electric field would not be infinite at the neutral points. This, in turn, implies there will be an electrical potential drop along two separated points along the separator connecting null points [*Sonnerup*, 1988]; confusingly, this potential drop along the separator is also referred to as a parallel potential drop, being a line integral of $\mathbf{E}$ along the separator, $\Delta\Phi = -\int_{\text{separator}} \mathbf{E} \cdot d\mathbf{s}$ (The dot product under the integral gives the component of $\mathbf{E}$ along the separator, which also is sometimes referred to as a parallel electric field). Numerous theoretical tracts suggest the pivotal role of $E_{\|} = \mathbf{E} \cdot \hat{\mathbf{B}}$ in the process of magnetic reconnection [*Vasyliunas*, 1984; *Siscoe*, 1988; *Vasyliunas*, 1988; *Schindler et al.*, 1988; *Hesse and Schindler*, 1988]. Quite apart from magnetic reconnection it had been realized quite early [*Pannekoek*, 1922; *Rosseland*, 1924] that electrical potential differences would be required in inhomogeneous plasmas to maintain quasi-neutrality and that these electric fields are of the type identified as ambipolar and would correspond, in general, to electric fields with components parallel to $\mathbf{B}$. Thus the defensible detection of $E_{\|}$ at the mV m^{-1} level is a strong indication that post-Hall MHD electrodynamics is underway and that the associated shorter length scales this requires are present in the plasma. As short scale lengths are required to understand collisionless reconnection, the novel $E_{\|}$ data to be presented in this paper are a major new tool in our search for the elusive diffusion region.

[10] The plan for this paper follows. After a brief overview (section 2) of the event context, using spectrograms and a selection of fluid parameters, magnetic field strength and GSM B_z variations, we document the near-null magnetic field region of the separator. We present the first direct detection of $E_{\|}$ at the magnetopause (section 3). Evidence is provided (section 3.1) that the sustaining force for $E_{\|}$ is the ambipolar contribution from the divergence of the electron pressure term. In section 3.2 we illustrate the strong tendency for the electron pressure to be enhanced within these magnetic depressions, consistent with recent multispecies and particle-particle theoretical models of collisionless magnetic reconnection. We have previously shown that this regime contains many rotational shear layers that pass the generalized Walén test [*Scudder et al.*, 1999]; thus the spacecraft on this day has reencountered rotational shear layers a number of times in several different places, passing the previously considered smoking gun test [*Sonnerup et al.*, 1995] of compatibility with magnetic reconnection "outside the diffusion region."

[11] Furthermore, we demonstrate that there are Walén tests done with electrons in the vicinity of, but outside of, the magnetic null point that have oppositely signed slopes, indicative of rotational shear layer traversals that are on opposite sides of the separator (We show in the sequel that the layer normals for these Walén tests are essentially pointed into the direction of the inflowing plasma, as required for them to stand in the flow). We illustrate (section 4.1) that the ion flow speeds exceed the Alfvén speed in the higher electron pressure (low $\mathbf{B}$) regions, while these same flows have weak Alfvén Mach numbers $\simeq 0.1$ when the P_e is reduced (in stronger $\mathbf{B}$ regions). These inflow Alfvén Mach numbers imply a reconnection rate that is similar to that deduced by the most modern multispecies codes that have modeled this layer (In the sequel we determine $\mathbf{E}_T$ and show that the plasma inflow rate and the "reconnection rate" via this component of $\mathbf{E}$ are consistent). Supra-Alfvénic parallel electron flow velocities ($M_{A,\|,e} > 5$) have also been detected (section 4.2) in these layers, as suggested by two-fluid, hybrid and full particle codes that describe collisionless magnetic reconnection and retain Hall and ambipolar physics in their generalized Ohm's law [*Pritchett et al.*, 1991; *Mandt et al.*, 1994; *Ma and Bhattacharjee*, 1996; *Shay et al.*, 1998].

[12] Detectable electron fluid pressure gradient drifts are expected as a corollary to the ambipolar scaling of the $E_{\|}$ measurements discussed in section 3.1. We demonstrate that there are times during this (and other) cusp traversal when the observed electric field drift and the electron fluid velocity perpendicular to the magnetic field agree (section 5.1 and

Appendix A3.5) and are different (section 5.2) at very high levels of confidence and of a size predicted by the ambipolar scaling of $E_{\|}$ that is simultaneously measured. In this way we confirm the importance of the electron pressure gradient drifts in these regions.

[13] We close (section 6) by providing the first experimental evidence of the necessary demagnetization of the electrons in the weakest field regions required by the *Vasyliunas* [1975] picture of ambipolar electric fields along the separator. The observed wide range ($>10^5$) of electron $\beta_e \gg 100$ signals the importance of retaining the ambipolar contributions to the generalized Ohm's law when describing reconnection.

[14] The electron thermal gyroradius in units of the anticipated electron inertial skin depth is determined by $\beta_e^{\perp}$; in the innermost region of the current layer this dimensionless ratio frequently exceeds 23. If, as expected, it can be shown that these same regions achieve electron inertial scale lengths, the present measurements would imply the thermal electrons are essentially unmagnetized there. We then show that there are significant indications that the electron pressure tensor is not gyrotropic within these layers, possibly a result of the demagnetization of the electrons and foreseen by *Vasyliunas* [1975].

2. Overview of 29 May 1996

[15] Polar's traversal of the northern cusp on 29 May 1996 occurred while a solar wind-borne magnetic cloud [*Farrugia et al.*, 1998] impinged on the magnetospheric system. The cloud presented a smooth, slow, and orderly rotation of the interplanetary magnetic field (IMF) that included a protracted period when it was nearly purely northward. By chance, Polar's cusp traverse to high latitudes on this day occurred when the IMF was nearly due north in the GSM system and the magnetopause was untypically compressed as a result of the high dynamic pressure of the cloud [*Russell et al.*, 1998]. Such a geometry favors merging (considering the antiparallel merging hypothesis [*Crooker*, 1979]) at sites just above the magnetic cusps in both hemispheres. Unlike most earlier missions that have probed the magnetopause by penetrating this surface along the radial direction, the Polar spacecraft essentially skimmed the magnetopause/boundary layers, moving more or less at right angles to the local magnetopause surface normal. Different portions of this particularly long cusp magnetopause crossing have been the subject of several previous papers [*Grande et al.*, 1997; *Savin et al.*, 1998; *Russell et al.*, 1998; *Urquhart et al.*, 1998; *Chandler et al.*, 1999; *Fuselier et al.*, 2000; *Onsager et al.*, 2001]. All but the last work listed have discussed the crossing from the magnetic field perspective in this region, in some cases together with discussion of the ion morphology. The first two papers used multiple spacecraft to testify to the wide spatial extent of the region encountered. The second paper illustrates that the Interball spacecraft did emerge into the unperturbed magnetosheath, unlike Polar. The last paper has probed the Polar observations using the distinctly shorter electron gyroradii scales. In all cases except the last paper, done in concert with the present studies, these reports infer the occurrence of reconnection removed from the spacecraft.

[16] The Polar "skimming" orbit provided a lengthy (over 4 hours) observation of the magnetopause and its vicinities (cf. Figure 1), apparently held in a rather stable position by the distended solar magnetic cloud. To provide the overall context for the detailed measurements to be considered in this paper, Figure 1 displays the omnidirectional ion and electron spectrograms and number density provided by the Hydra instrument for this period [*Scudder et al.*, 1995], the magnetic intensity and GSM B_z component from the MFE instrument [*Russell et al.*, 1995], and the variation of orbital parameters during this pass near local noon.

[17] The density is elevated during the cusp interval. However, in the early part of this cusp excursion by Polar the local magnetic field is southward in GSM, while after 0407:36 UT the local magnetic field turned northward even as the Polar spacecraft is moving up toward higher magnetic latitudes. This northward field interval is consistent with the northward field being imposed on the magnetosphere by the impinging magnetic cloud. During the cusp traversal, between 0315 and 0715 UT, numerous deep depressions of B were intercepted. Weak fields are first seen at 0435:00 UT, and many repeated deep depressions in B occur later in this interval. This sequence of magnetic depressions culminates at 0704:29.45 UT, where the field strength vanishes, being consistent with magnetometer zero-level uncertainties.

[18] The time resolution of the measurements considered in this paper depends on the detector's capability and, to some extent within the plasma instrument, what parameters are being inventoried. The magnetometer data are reconstructed to 54 Hz. The electric field measurements are transmitted at 40 Hz. The plasma electron density and trace of the pressure tensor are known at 1.15 s if necessary. The fastest information about odd moments including flows is 4.3 s for electrons; these results depend on the plasma being gyrotropic. Model independent ion and electron moments at the slower 13.8-s cadence are available for all quantities up through the heat flux vectors.

[19] This paper will consider the plasma and **E** and **B** field data between 0636 and 0715 UT, where the deepest depressions and biggest field variations were observed. An overview of the plasma and field measurements is given in Figure 2.

[20] In this interval, there are numerous traversals from strongly northward to southward magnetic fields, as well as a large number of very strong depressions in the magnetic intensity. The plasma flows also show strong variations in the region. The electron pressure is highly structured, being high on the sunward side of the boundaries and having unusually strong gradients at and across the changes in B_z. These precipitous gradients play an important role in the description of collisionless reconnection as we explore below.

[21] The weakest magnetic field, observed at 0704:29.45 UT, had time variations of its components in spacecraft payload components that are illustrated in Figure 3.

[22] The horizontal dashed lines indicate the ± 1, 2σ estimates of the absolute precision on each measurement axis. The vertical errors indicate the imprecision of the magnetic field component's reconstruction at this high data rate (cf. Appendix A1). Given the measurement uncertainties, these data demonstrate that the deepest depression in the magnetic field strength on this pass was very nearly a

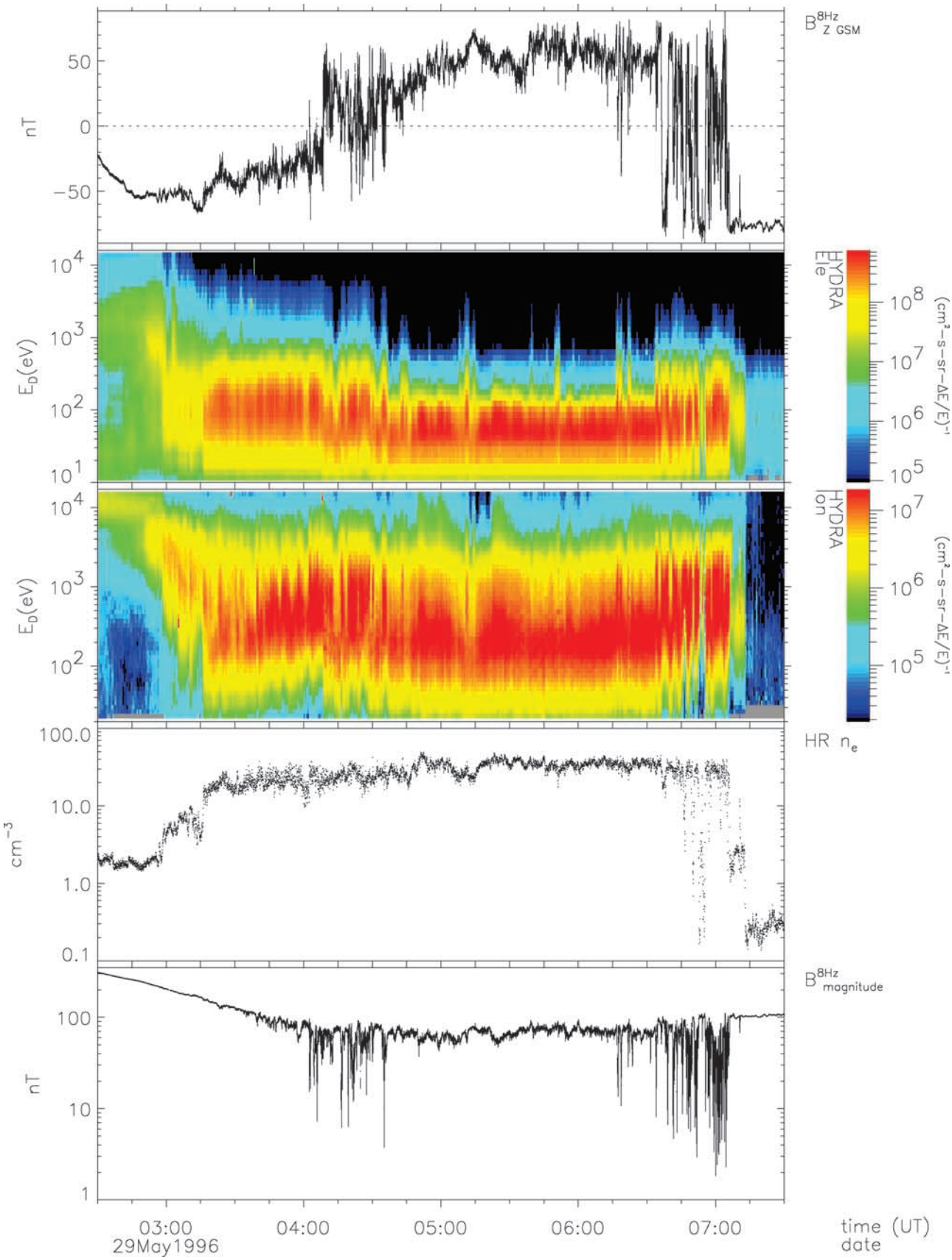

Figure 1. Traditional view of cusp traversal in spectrogram format.

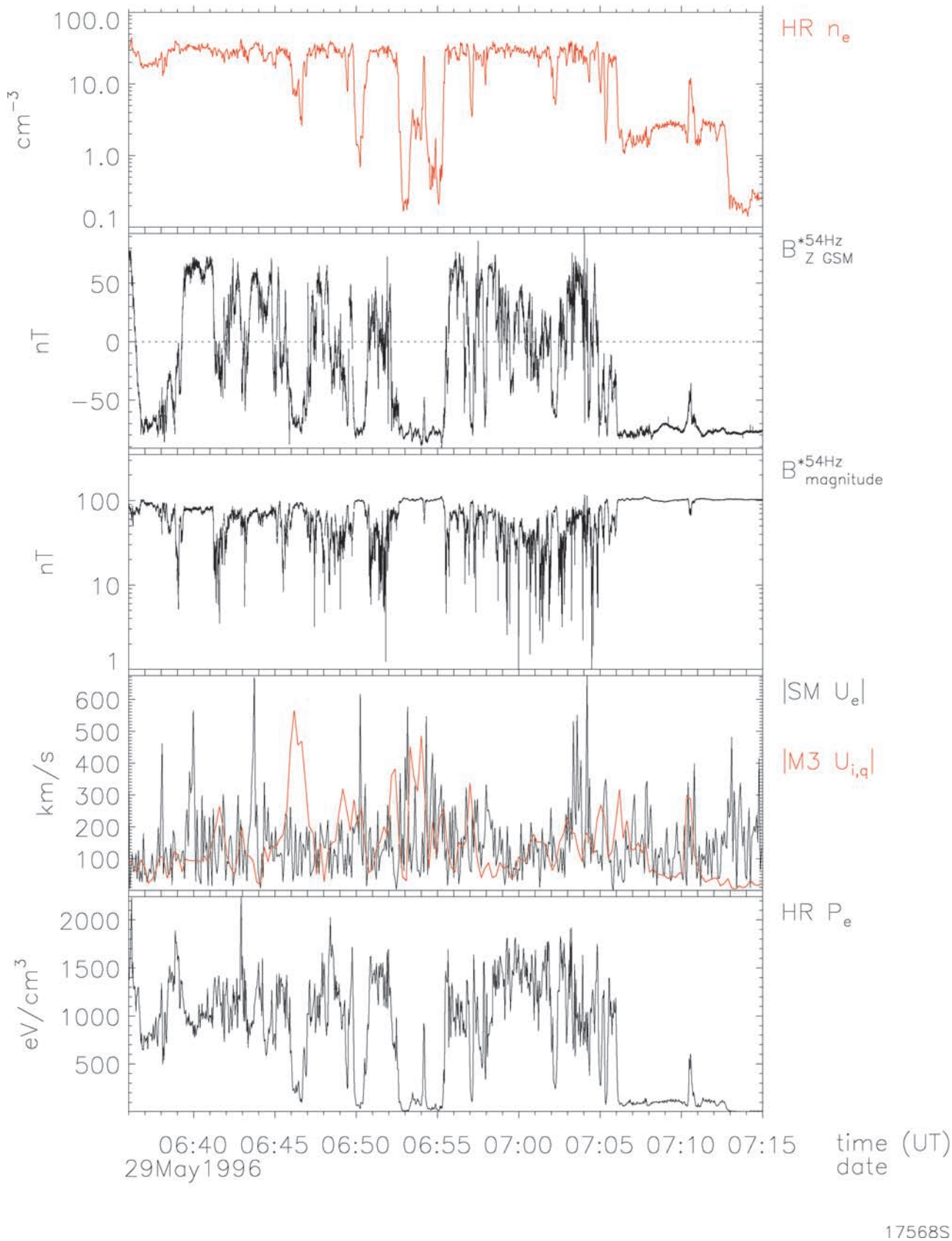

Figure 2. Panels from the top: electron density (1.15 s), GSM B_z(54 Hz), |**B**|(54 Hz), electron (black, 4.3 s) and ion (red, 13.8 s) bulk speed, and electron pressure profile (1.15 s).

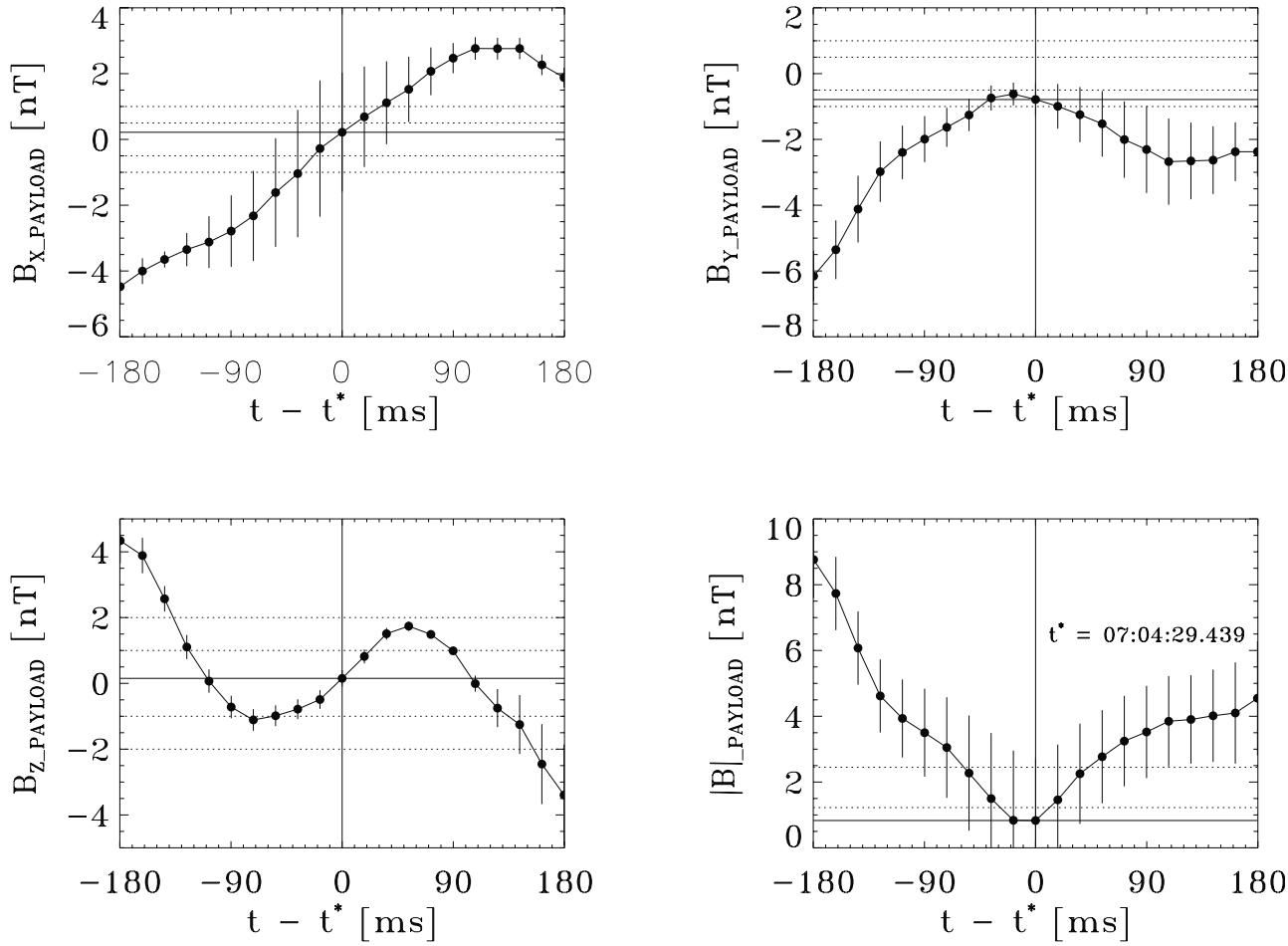

Figure 3. Reconstruction of the B(t) at 54 Hz near the weakest field interval during this 4 hour cusp crossing. Time units are epoch time in milliseconds before or after 0704:29.449 UT. Error flags reflect the estimates of reconstruction uncertainties discussed in Appendix A. A companion paper illustrates that the spatial interval of this time snapshot is twice the local electron inertial length.

true null in the field. If such a region were a separator traversal, it would be classified as a separator without "guide" field, since the magnetic field strength at the "site" cannot be defensibly argued as nonzero. If this layer were the expected separator of theory, its spatial extent of this entire time interval should be $\sim 2c/\omega_{pe}$.

[23] While deeply depressed field regions at the magnetopause have been previously reported [*Sonnerup and Cahill*, 1968; *Aubry et al.*, 1971; *Neugebauer et al.*, 1974; *Gosling et al.*, 1986; *Gosling et al.*, 1990; *Paschmann et al.*, 1986; *Dunlop et al.*, 1999], the unprecedented suite of correlative measurements that accompany the present observations permit a new diagnosis of these structures and allow us for the first time to identify the separator with its framing separatrices, the dynamics in the layers near this separator, as well as other features and scales of the diffusion region. As discussed in the introduction, it is the detection of spatial scales that sets our identification apart from previous observations of magnetopause crossing with depressed magnetic fields in their interior.

[24] A critical part of the new instrumentation available with GGS-Polar is the 3-axis electric field observations of the electric fields investigation (EFI) instrument [*Harvey et al.*, 1995] that permit the direct measurement of $E_{||}$ within these regions for the first time (On previous missions, two axis **E** measurements have been used together with the presumption that $\mathbf{E} \cdot \mathbf{B} = 0$ to compute the third component of **E**. Consequently $E_{||}$ was defined to vanish). The vector electron bulk velocity, $\mathbf{U}_e$, is the other newly observed quantity in the present discussion of the magnetopause current layer and has been determined from the Hydra measurements [*Scudder et al.*, 1995]. Since the electron fluid usually affords diagnostics of magnetic field line motion [*Scudder*, 1997], these additional measurements permit an empirical comparison of the $\mathbf{E} \times \mathbf{B}$ velocity with the cross-field components of the electron bulk speed, $\mathbf{U}_{\perp,e}$. Important information on the scale lengths present in these layers and the importance of electron pressure variations in their description can thus be derived. Using these data, we will develop arguments that these depressions in **B** are not solely the result of thick, ion scale structures moving rapidly over the spacecraft but are structures with a range of inertial length scales, including those surmised over 25 years ago by *Vasyliunas* [1975] to be important in the layers about the separator of collisionless reconnection. The importance of the pressure divergence also suggests a cause for the reported parallel electric field

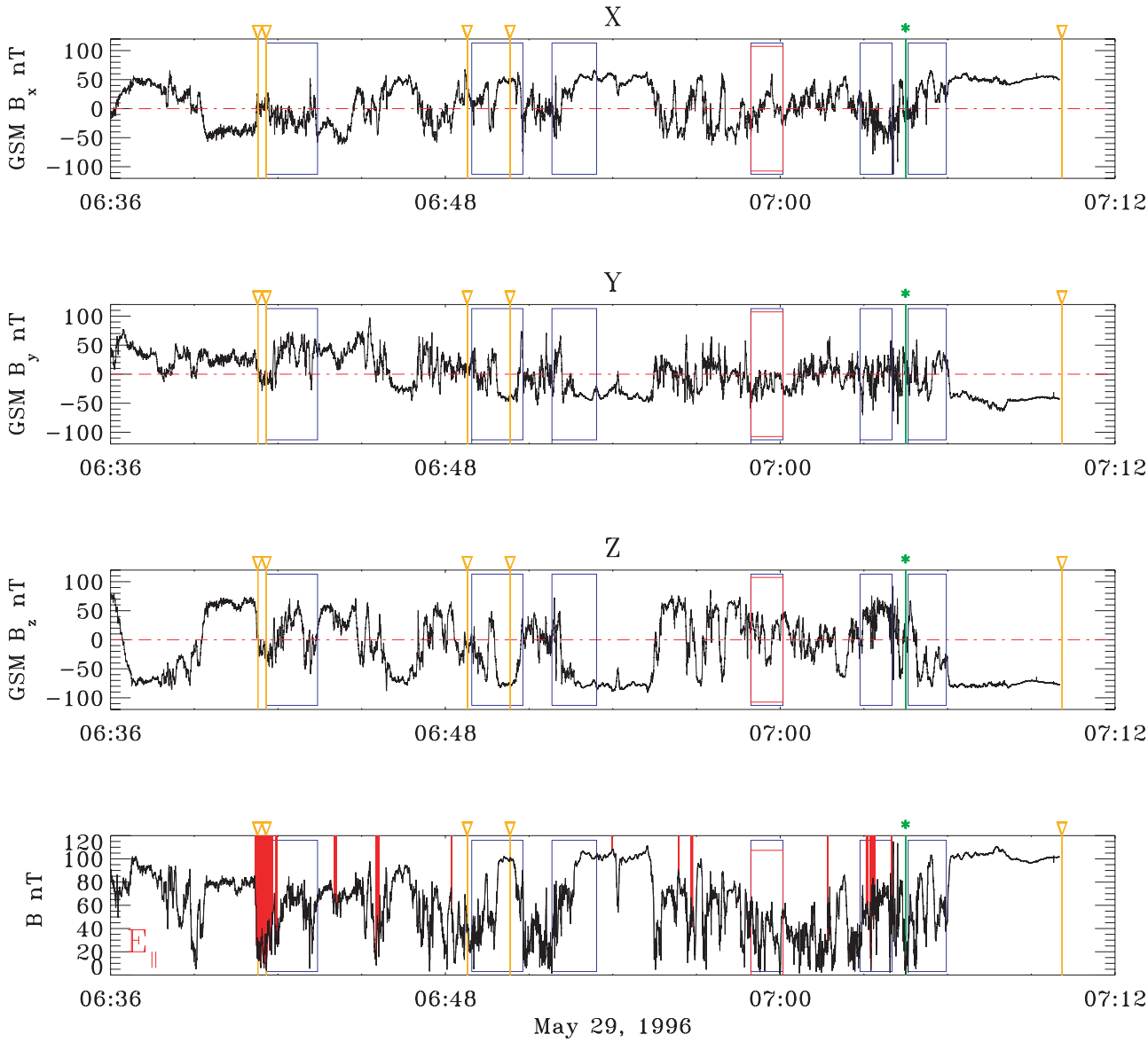

Figure 4. Magnetic field at 54 Hz in GSM coordinates between 0636 and 0710 UT, 29 May 1996. The fourth panel with the field magnitude also indicates with vertical red lines the locales where $E_{||}$ detections of very high quality are reported in this paper. In some regions, these lines are so dense that intervals of time appear painted red by the juxtaposed lines. Blue rectangles indicate where successful Walén tests with electrons have been previously reported [*Scudder et al.*, 1999]. One rectangle has a red-inscribed rectangle. This red-blue rectangle indicates the Walén interval where the Walén slope, $\alpha = -1$, indicative of RD traversal above the separator for an impinging northward IMF. The orange lines (with ∇ call-outs) indicate the locales where the data discussed in Figures 11–15 were obtained. The thick green line (with the asterisk call-out) is centered at the magnetic null illustrated in Figure 3.

and can also produce pressure gradient drifts in the electron fluid's cross-**B** drift, $U_{\perp,e}$. In such regions the electron cross-field drift would not always be equal to the electric drift, $c\frac{\mathbf{E}\times\mathbf{B}}{B^2}$; we provide, as well, first empirical demonstrations of this effect in the vicinity of the separator.

[25] With inertial scales suggested, further steepening of scale lengths of the current to the electron inertial length would also explain the first observations reported here of departures from cylindrical symmetry of the electron distribution function in the electron's bulk velocity frame of reference. Such departures could support the needed electric field along the separator at the magnetic null in the absence of any form of resistivity. We illustrate that the local thermal electron gyroradius at and near the separator is an order of magnitude larger than the electron inertial length (pushing the ion inertial length), a necessary prerequisite for such a description.

3. 0636–0715 UT on 29 May 1996

[26] We concentrate our discussion on the interval between 0636 and 0715 UT illustrated in Figure 4. This

interval has been selected because it includes multiple deep magnetic depressions shown in Figure 1 and because it also excludes times of various known experimental ambiguities (cf. Appendix A2). In particular, all particle and field data in this interval have been excluded when there are suggestions that the preamplifiers in the EFI subsystem might be oscillating (precise time exclusions are defined in Appendix A2).

[27] The three components of and magnitude of **B** are displayed in Figure 4. The blue boxed intervals in each panel indicate time domains where Walén tests of the type previously reported by *Scudder et al.* [1999] have been successful. The Walén intervals are identified both before and after the identified separator traversal indicated by the green asterisk in Figure 2. The Walén interval indicated with the red inner box is unusual in this interval having a Walén slope of -1, while the others in this interval are all very close to +1, using the electron formulation discussed by *Scudder et al.* [1999]. Opposite Walén slopes are required in the simplest interpretation of the external RD waves standing on either side of the separator. The sign of the slope, α, of the Walén test is proportional to the ratio of the normal flow velocity across the RD, V_n, and B_n, the component of **B** along the RD normal. A negative α implies the mass flux and the normal component of **B** are opposed versus being aligned when it is positive. The predominant sign of α in this 40-min interval is positive, indicative of mass flux parallel to the normal component of **B**, thus of observations below the separator for a northward external magnetic field. Conversely, the $\alpha = -1$ interval requires the mass flux, which is presumably still toward the earth, to be opposed to B_n (which must have changed sign), as would have occurred intercepting an RD above the separator. The time order of occurrence in these data of these oppositely signed slopes is not consistent with the observer's world line sweeping from below the separator to above the separator in a monotonic way. There is considerable evidence that the location of the separator is not fixed in inertial space for this time interval but is moving about. This motion will be quantified in the sequel. For the present the coordinate independent character of the Walén test provides evidence of topology in the sense indicated above.

[28] Distributed throughout this interval are locales where $E_{\|}$ has been experimentally measured for the first time within the magnetopause current layer. The temporal incidence of these detections described below are indicated in the fourth panel of Figure 4 with the red lines that connect the local value of B at the point of detection and the upper border of the panel (On the overview scale of this picture, these separate lines appear to merge into continuous intervals of red beneath the fully resolved magnetic field trace). The determined parallel field strengths range from a fraction of a mV m^{-1} to over 8 mV m^{-1}. A histogram of the parallel field sizes are illustrated in Figure 6e, and the longest contiguous interval of certified parallel electric fields is depicted in Appendix A2, Figure A4.

[29] Determinations of $E_{\|}(t)$ from the EFI measurements are admitted to physical interpretation only after they have passed a number of internal consistency checks from the 3-axis measurement system of EFI (cf. Appendix A2). Accordingly, no inference should be drawn from these measurements about the size or presence of $E_{\|}$ in regions between the red lines in the fourth panel of Figure 4, which highlight the locations where $E_{\|}$ has been unequivocally detected. The certification of these electric field measurements was performed without consideration or correlative knowledge of the contemporaneous plasma measurements or magnetic field strength. These consistency checks suggest that these signals are associated with the elusive parallel electric field necessary to forestall the conclusions of ideal MHD. In view of the stringent screening applied to candidate $E_{\|}$ measurements, we note that there may be other instances in this interval where significant $E_{\|}$ exists. They were excluded in the analysis below to ensure the overall integrity and independence of the detections of those data that have passed the rigid tests of internal consistency discussed in Appendix A2.

3.1. Ambipolar Character of $E_{\|}$

[30] As these $E_{\|}$ measurements are at present unique at the magnetopause, we seek to organize them with other physical or theoretical estimates of their size. It has previously been suggested that the parallel electric fields required for magnetic reconnection could be supported by the ambipolar electric field opposing the electron pressure force [*Vasyliunas*, 1975] in the absence of resistivity or electron inertial effects. These ambipolar electric fields were suggested to become important when the fluid dynamics required spatial scales

$$L_{VMV} \simeq O(1)\beta_e^{1/2}\frac{c}{\omega_{pi}} = \beta^{1/2}\frac{c}{\omega_{pi}} \equiv \rho_s \tag{1}$$

and were suggested that they maintain the electric field along the separator when the electron pressure tensor is no longer gyrotropic. Other authors have referred to this scale by the name ρ_s [*Pritchett et al.*, 1991; *Zakharov and Rogers*, 1992; *Ma and Bhattacharjee*, 1996; *Shay et al.*, 1998]. An alternate view of this scale length is that it is the distance a fluid element can travel as an acoustic disturbance in an ion Larmor period, namely, $\rho_s = C_s/\Omega_{ci}$, where C_s is the ion sound speed and Ω_{ci} is the ion cyclotron frequency, which reduces to the Vasyliunas result when $\gamma_e T_e = \gamma_i T_i$; $\gamma_e = 1$. A detailed derivation of this scaling result is given by *Zakharov and Rogers* [1992].

[31] When the spatial scales formed in the reconnection layer are of this size, the parallel electric field from the ambipolar term can be estimated as

$$|E_{\|}| \le |E_{ambi}| = O(1)\frac{P_e}{en_e\rho_s}. \tag{2a}$$

Upon inserting the ρ_s scale, equation (2a) becomes

$$|E_{\|}| \le O(1)\sqrt{\frac{kT_e}{2m_ic^2}}|B| \equiv E_{VMV}. \tag{2b}$$

We refer to the right-hand side of equation (2b) as the "Vasyliunas" conjectured limit, E_{MVM}, for $|E_{\text{ambipolar}}|$. This same limit is always an upper limit for the expected perpendicular ambipolar electric field that would determine the electron pressure gradient drift, namely

$$|E_{\perp}| \le O(1)\sqrt{\frac{kT_e}{2m_ic^2}}\,|B|\,. \tag{2c}$$

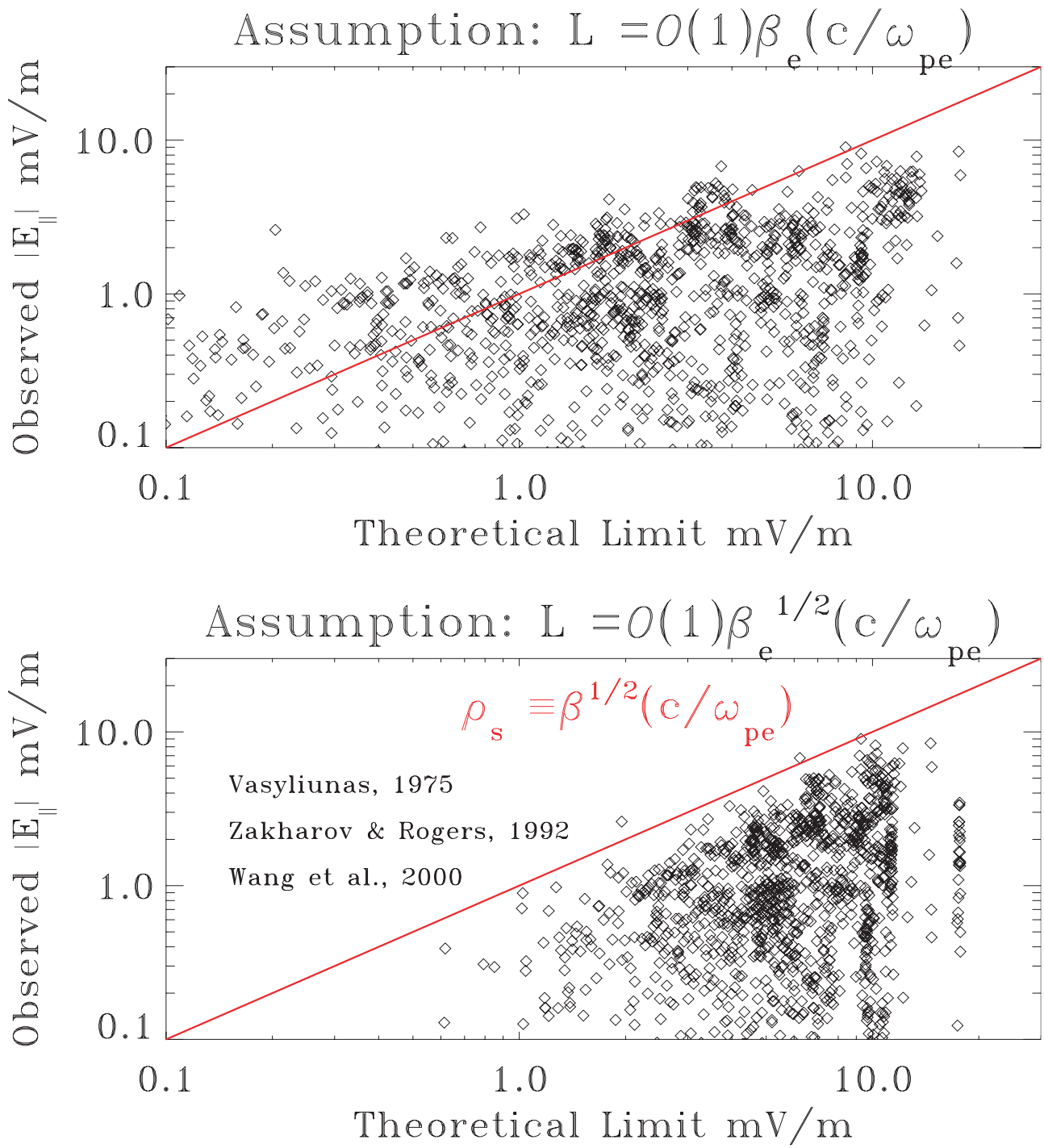

Figure 5. Scatter plot of $E_{\|}(t)$ versus two theoretical limits for its size, assuming the pressure gradient scales like $L = \beta \frac{c}{\omega_{pe}}$ (first panel) or as $L = \beta^{\frac{1}{2}} \frac{c}{\omega_{pe}}$ (second panel). Points below the diagonal red line indicate consistency with asserted scaling. Almost all certified $E_{\|}$ points from this study are consistent with the ρ_s scaling exhibited in the second panel.

At different times in this paper we will use E_{VMV} as a useful bound for either $E_{\|}$, which is almost surely ambipolar in character, or as a bound for the perpendicular part of **E** contributed by the ambipolar pressure divergence.

[32] Empirically, we identify that $O(1) \simeq \sqrt{14} = 3.7$ by examining Figure 5, which illustrates the location of certified $E_{\|}$ events of this study versus two predicted scalings of their limiting values indicated in the two panels of Figure 5. The horizontal axis of both panels is the theoretical size of the ambipolar electric field assuming the pressure divergence scales as (a) $\beta \frac{c}{\omega_{pe}}$ (first panel) or (b) as the $\rho_s = \beta^{12} \frac{c}{\omega_{pe}}$ scaling (second panel) asserted by Vasyliunas. Data points in this figure have coordinates (E_{bound}, $E_{\|}$), so that points consistent with the asserted bounding form would satisfy

the inequality $E_{\|} \leq E_{\text{bound}}$ and be below the red line drawn in each panel. This figure demonstrates that the ρ_s scaling is indeed more consistent with the new $E_{\|}$ measurements than the scaling assumed in the first panel of Figure 5. The scaling hypothesis of the first panel arises from the electron momentum equation without reconciling it with the overall energy equation and ion dynamics. The second panel requires a full two-fluid discussion not advanced by Vasyliunas but recently published *Zakharov and Rogers* [1992].

[33] Equality in equations (2a) and (2b) occurs when the pressure divergence is antiparallel to the local magnetic field direction, when the perpendicular part of the pressure divergence would be zero. Conversely, when the parallel electric field would be zero, the entire bound would be available for providing a cross-field force and hence drift to the electron gas that would be in vector addition to the electric drift it experiences. The limiting size of E_{VMV} can also be written as

$$E_{\|}^{VMV} \leq \sqrt{7}\frac{C_{s,e}}{c}|B|, \tag{3a}$$

where $C_{s,e}$ is the isothermal ion sound speed involving the electron temperature alone. The average total isothermal acoustic speed is

$$C_s \equiv \sqrt{\frac{(kT_e + kT_i)}{m_i}},$$

which for this data set is approximately $\sqrt{8}C_{se}$. Within the precision of the estimate of the $O(1)$ term in this Figure, equation (3a) becomes

$$E_{\|}^{VMV} \leq \frac{C_s}{c}|B| \tag{3b}$$

The Vasyliunas scaling is consistent with a maximum pressure gradient drift at the isothermal sound speed, C_s. It is the formulation via equation (3b) that explains the labeling of L_{VMV} with ρ_s, a scale length associated with the (ambipolar) sound speed.

[34] Finally, it should be emphasized that the onset of such physics introduces a new possibility and hence scale for the electron support of currents. Until the mechanical scale reaches the ρ_s scale, the electric drift of magnetized electrons and the partial demagnetization of the ions define an ion inertial scale for current. With the sharper ρ_s scale (possible when $\beta_e < 1$) the current can be intensified by the electrons pressure gradient drift in addition to the contribution by electrons while electric drifting. Provided $\beta_e < 1$, the ρ_s scale provides a way for the current layer to develop stronger currents and inner scales shorter than the initial ion skin depth of the current. With increasing $\beta_e > 1$ the ρ_s scale is no longer shorter than the ion skin depth, and the electron skin depth is the remaining shorter nonresistive scale available for intensifying the current scales. So long as $1/1836 < \beta_e < 1$, the ρ_s scale is intermediate between the electron and ion skin depths. We illustrate in Figure 6f that the incidence of β_e for these events is strongly bounded by these limiting values, which supports the association of $E_{\|}$ with the occurrence of the "intermediate" ρ_s layer of the vicinity of the separator.

[35] In the absence of a guide field a neighborhood of the separator always exists in which the ambipolar term is more important than the unipolar field. This condition reduces to the C_s becoming larger than the local Alfvén speed. In the present data where $T_e = 20$–40 eV, where $T_i/T_e \simeq 10$ this regime occurs whenever $B < 37$–39 nT and represents 59% of the time when **B** is sampled in this interval. At still larger magnetic field strengths the ambipolar drift could still be present but would not dominate the local Alfvén speed.

[36] If the mechanical system of the reconnection layer developed spatial scales in the vicinity of the separator that were no shorter than the ρ_s scale, the ambipolar parallel electric field would be organized according to

$$E_{\|} \simeq E_{VMV}\cos\Psi, \tag{4}$$

where Ψ is the spatially varying angle between the electron pressure force, $-\nabla \cdot \mathbf{P}_e$, and the magnetic field, **B**. Entry into pressure gradients with even shorter d_e scales or time-dependent electric fields might be indicated by ambient $|E_{\|}| > E_{VMV}$. With our scaling we have a few parallel fields in our biased sample of validated $E_{\|}$ measurements that exceed this limit. We discuss the spatial location of our $E_{\|}$ observations relative to the separator in the sequel.

[37] In Figure 6a we plot the observation frequency of the dimensionless parallel electric field during this interval based on the Vasyliunas scaling argument. These dimensionless ratios have a distribution frequency almost exclusively (1228 out of 1231) at or below unity, consistent with the argument that their distribution is bounded from above.

[38] Using those readings with ratios less than or equal to unity, we determine the implied distribution frequency of the angle Ψ. As a corollary of the information in Figure 6a, the Ψ distribution in Figure 6b is strongly peaked near 90°. Figure 6c depicts the distribution of implied pressure gradient drifts that would attend the $E_{\|}$ observations under the ambipolar field limit suggested by the data. Figure 6d illustrates and contrasts the percentage distribution of frequencies throughout this interval of $|\mathbf{B}|$'s sampled in this interval where $E_{\|}$ has been detected (red) with the occurrence frequency of the magnetic field magnitudes themselves (black). The mode and means of B where $E_{\|}$ has been certified are noticeably lower than the corresponding mode and mean for **B** in the time interval that was searched. It should be emphasized that the parallel electric fields were identified without knowledge of the magnetic field strength, just its direction. The modal value of **B** where the $E_{\|}$ fields have been certified is 20 nT, decidedly smaller than the ambient 80–110 nT fields on either side of the current-carrying layer. 56% of the $E_{\|}$ certified events occur below the weak magnetic field regimes ($|\mathbf{B}| < 39$ nT) necessary for the ambipolar term to overpower the unipolar term. Figure 6e illustrates the distribution frequency of the observed $E_{\|}$'s used in this paper. The distribution is peaked at small values, but when it is realized that the unipolar electric field in the magnetosheath at 100 km s^{-1} and 80 nT is 8 mV m^{-1}, the detection of even 0.5 mV m^{-1} with cross checks is a very strong parallel electric field. Within Figure 6f, a summary is made of the β_e that accompanies

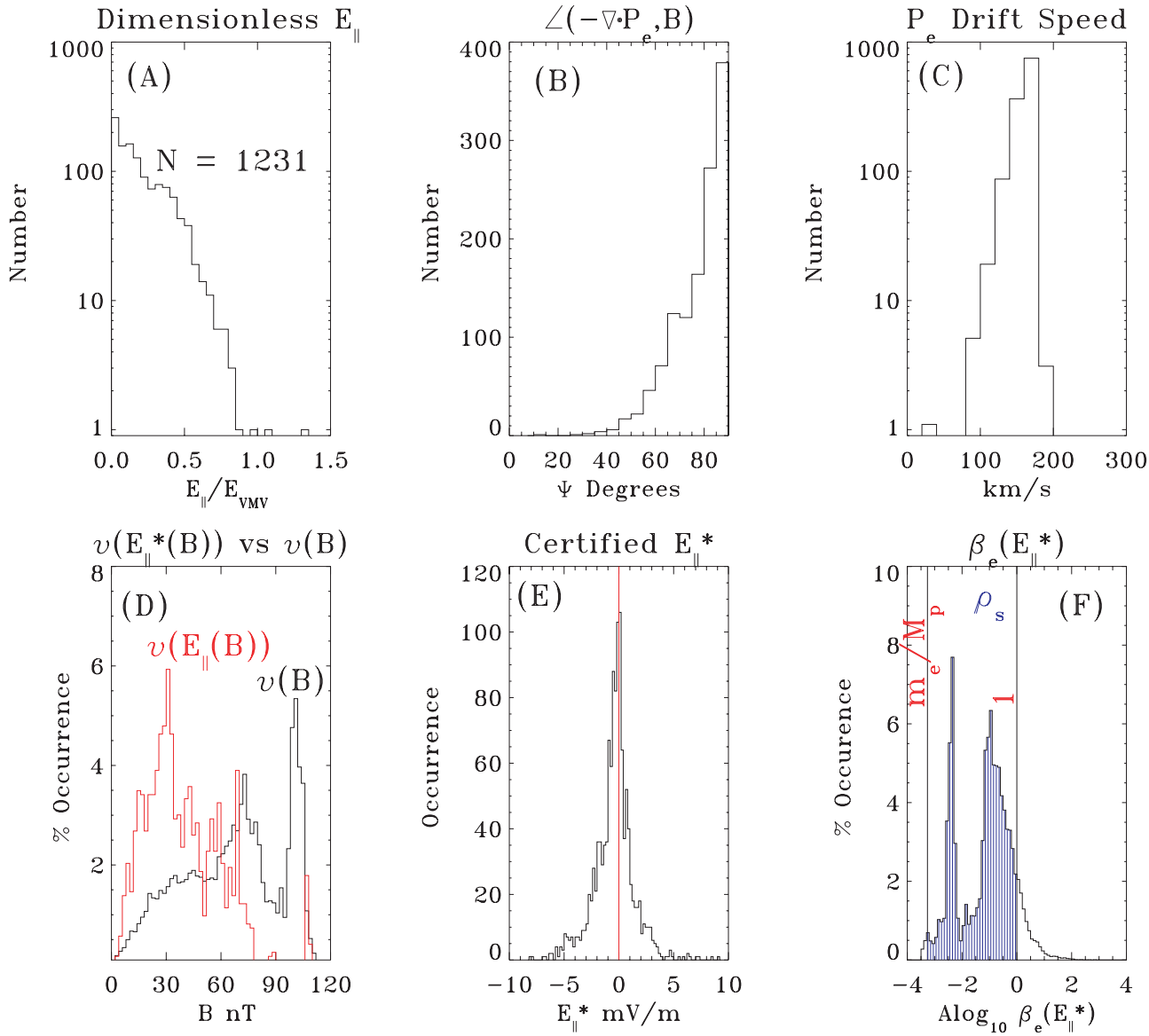

Figure 6. (a) Distribution frequency of dimensionless $E_{*\|}/E_{VMV}$, where $E_{*\|}$ is a certified parallel field observation. (b) Implied frequency distributions of angle Ψ between electron pressure gradient force and B. (c) Implied frequency distribution of pressure gradient drifts implied by $|\mathbf{E}_{\perp}| = \left(E_{VMV}^2 - E_{\|}^{*2}\right)^{\frac{1}{2}}$. (d) Percent frequency distribution of certified $E_{\|}^{*}$ (red) and all $|\mathbf{B}|$ (solid) with $|\mathbf{B}|$ between 0636 and 0710 UT. (e) Observed distribution of $E_{\|}^{*}$ from the 1231 events in Figure 6a. (f) Distribution of β_e that labels the sites where $E_{\|}^{*}$ has been certified in this study. The blue shaded region corresponds the regime of β_e where the ρ_s scale is nested between the electron and ion inertial lengths and hence distinct from them; a large majority of the intervals where $E_{\|}^{*}$ has been detected are between these limits.

the certified parallel electric fields, $E_{\|}^{*}$. The occurrence frequencies are almost completely localized between m_e/M_p and unity, precisely as required by the theory, occurring at intermediate and distinct scale between the electron and ion skin depths. The peaks of the distribution of β_e's are well removed from either limit with the principal peak of order $\beta_e < 10^{-2}$, which gives the typical ρ_s scale of this interval to be an order of magnitude thinner than the ion skin depth.

[39] From this organization we conclude that Vasyliunas' 25-year-old picture of the layer could indeed explain these newly certified $E_{\|}$ measurements in these layers at the magnetopause. The 1228 readings that satisfy the Vasyliunas limit should be considered primary experimental evidence for passage through that part of the diffusion region associated with the nonideal MHD "intermediate ρ_s scale" discussed in the section 1. We believe this corroborated data and that of Figure 3 represent the first empirical argument for penetration of the diffusion region of collisionless reconnection theory per se; it is also the first experimental evidence that the ambipolar-moderated form of collisionless magnetic reconnection might be the correct way to break the "frozen flux" approximation at the magnetopause, rather than wave particle effects or electron inertial resistivity

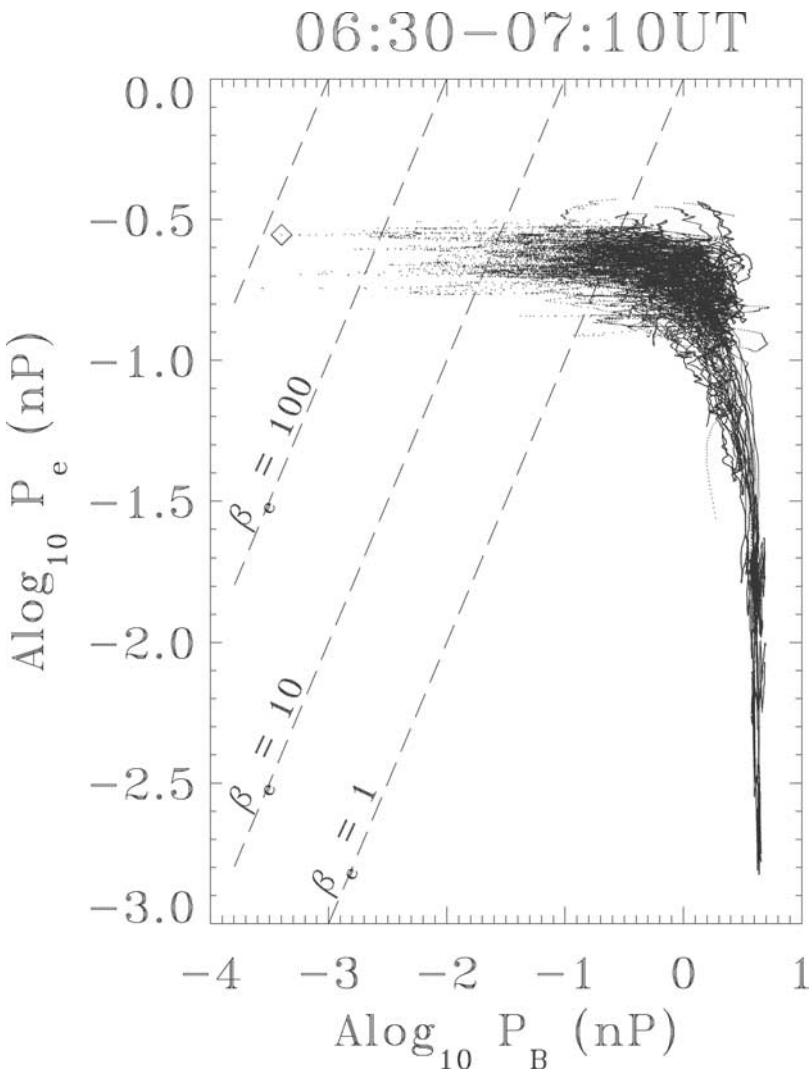

Figure 7. Observed anticorrelation of the observed electron pressure, $\frac{1}{3}TrP_e$, with concurrent magnetic pressure, $P_B = \frac{B^2}{8\pi}$. Integral powers of 10 of the electron β_e are also indicated. All data between 0636 and 0710, excluding brief intervals discussed in Appendix A2. Triangle highlights data point where a peak electron $\beta_e \simeq 80$ was recorded.

alone. In the language of the modelers, tensorial ambipolar-moderated Hall MHD would be essential to the description of these layers, a point that has recently been affirmed with full particle simulations [*Hesse et al.*, 1995; *Shay et al.*, 2001; *Hesse et al.*, 2001; *Pritchett*, 2001] and reviewed theoretically by *Scudder* [1997]. This is not to say that electron inertial effects might not also be important in the layer as we suggest in section 6. We will return to the evidence of electron skin depth structures in a later portion of this paper and in its sequel.

3.2. Detection of the Pressure Ridge

[40] Another indication of proximity of these observations to the separator line would be the detection of an inverse variation between the electron pressure, P_e, and that of the magnetic field, P_B. Successive depressions in the magnetic field during this event might be multiple close passes with the current sheet that is nonetheless nearly stationary in its own frame of reference. In the two-fluid picture of the reconnection layer [e.g., *Ma and Bhattacharjee*, 1996], an electron pressure ridge occurs with principal gradients along the inflow and outflow directions, with a maximum pressure on the current layer, with a mild (1%) saddle point centered on the separator. In the inner region where B is weakest, the mechanical equilibrium with the weak inflows is essentially an electron gas pressure variation in anticorrelation with the eroded magnetic pressure. The scale of the variation of B in the inner region is so short that simulators ignore the ion dynamics since they are not able to respond. Using 1.15-s estimates of the trace of the electron pressure variation, we illustrate the variation of the electron pressure with magnetic field pressure in Figure 7. As the electron pressure varies much less rapidly than does the magnetic pressure or the parallel electric field, the necessary $P_e(t)$ has been interpolated to the resolution of the magnetic field data.

[41] This variation statistically suggests that the temporal variations observed in Figure 4 are much more coherent

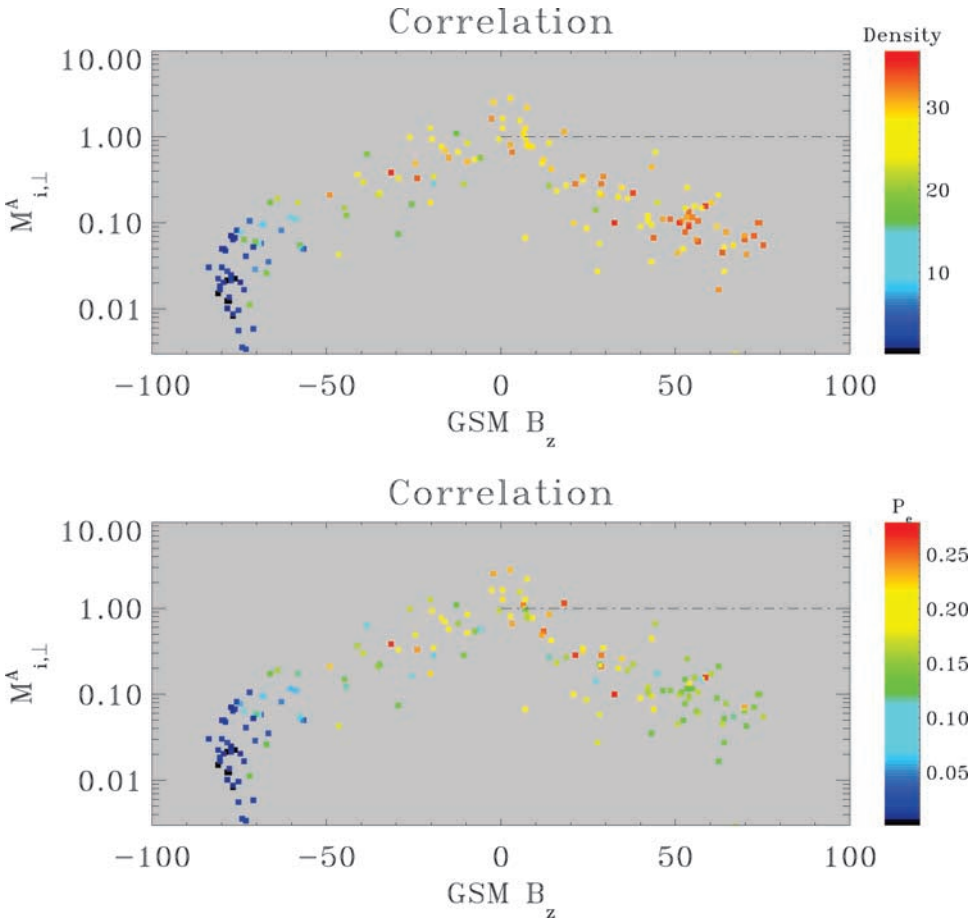

Figure 8. First panel: Variation of ion perpendicular Alfvén Mach number $M^A_{i,\perp}$ with GSM B_z, color coded by ambient electron density. Second panel: Same correlation as in first panel but keyed here by electron pressure.

than a plot versus time (as in Figure 2) would suggest. Figures 7 and 4 suggest that a spatially varying structure, coherent in time, is being swept back and forth over the spacecraft. The skimming trajectory of Polar at this high-latitude magnetopause crossing is an important consideration for this possibility. The strongest electron pressure gradients do not occur at the weakest magnetic pressures but at intermediate and high magnetic pressures. However, the log-log character of Figure 7 hides the factor of 2 variations in pressure that are present in the weaker field regimes where most of the reported $E_{\|}$ events have been found.

[42] Figure 7 suggests an anticorrelation between field and electron plasma pressure that appears rather reproducible with the large number of points included in its construction. To convert Figure 7 to spatial gradient information, the spatial variation of one or the other of these profiles is required.

[43] Accordingly, the vicinity of the electric field measurements discussed above does possess collocated electron pressure gradients. In the simple picture of magnetic reconnection without a guide field, B goes to zero on the separator. According to the Vasyliunas ambipolar bound, E_{VMV} in this limit also goes to zero, as does the spatial pressure gradient as the pressure profile approaches its minimax saddle point at the magnetic null (Strictly speaking, the pressure at the separator is a very mild saddle point in pressure, that is so shallow, according to current models, that it may not be perceptible with observations; Z. Ma, personal communication, 1999). In any case the separator is suggested to be accompanied by a higher than ambient saddle point in the electron pressure, even though the absolute maximum electron pressure is suggested to be displaced on either side of the separator along the Chapman-Ferraro current layer.

4. Supra-Alfvénic Ion and Electron Mach Numbers

4.1. Ion flows

[44] We illustrate in Figure 8 the organization of the local ion Alfvén Mach numbers as organized by the simultaneous observations of GSM B_z, a proxy for position of the S/C along the normal to the current layer. As the imposed interplanetary magnetic field (IMF) is nearly due north in this interval, positive (negative) B_z corresponds to the most sunward (earthward) sides of the layer. The first panel shows data keyed by the local density and also nicely shows the incident sub-Alfvénic inflow with (reconnection rate) $M^A_{i,\perp} \simeq 0.1$ on the sheath (northward B_z, higher density)

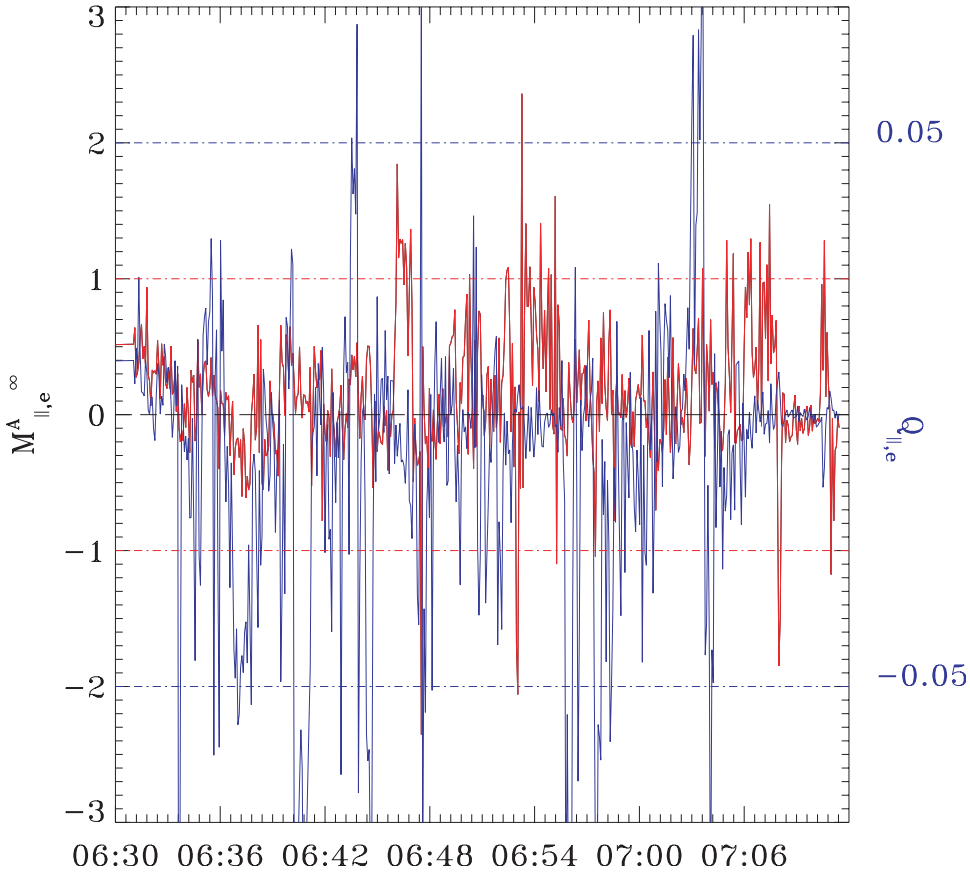

Figure 9. Variation of $Q_{\|,e}$ (blue) and $M^{A,\infty}_{\|,e}$ (red) between 0630 and 0712 UT. When these sheets are resolved, there is a tendency for the highest Alfvén Mach number flows to be displaced from the heat flux sheets, previously argued to be signatures of the separatrix.

side and a cluster of similar values on the magnetospheric side. These ion flow measurements are available at 13.8-s resolution. At the current sheet crossing, the data are clearly consistent with $M^A_{i,\perp} \simeq 1$ flows. The density maximum occurs on the sheath side rather than at the current sheet crossing, giving a sense of the intrinsic asymmetry across the current layer. The second panel presents the same data, keyed with the electron pressure, showing the enhanced electron pressure as the z component of **B** weakens.

[45] Not only are trans-Alfvénic ion flows detected in this regime, but they also occur only at highest values of $\frac{1}{3}TrP_e$. Conversely, weak ion flows with $M^A_{\perp,i} < 1$ are seen in the lower pressure regimes and in the increasing P_e regimes, but not during the highest P_e values recorded in this interval. In the high electron pressure regions the local ion $M^A_{\perp,i}$ is generally of order unity, with occasional readings exceeding unity.

4.2. Electron Flows

[46] Supra-Alfvénic parallel electron bulk flows are a steady state feature near the separatrices of two-fluid, hybrid and particle- particle models of collisionless reconnection [*Pritchett et al.*, 1991; *Mandt et al.*, 1994; *Ma and Bhattacharjee*, 1996; *Shay et al.*, 1998]. Narrow but large amplitude electron Mach number flows have been detected in the Hydra data set for this event with extreme local values of $|M^e_{A,\|}| \simeq 5$. Maximum parallel electron Mach numbers deduced are possibly limited by the 4.6 s temporal resolution of data. Without knowledge of their spatial extent we cannot model the maximum Mach numbers possibly present by the detected flows but can only note that the detected numbers could be lower limits if such larger flows were in very thin sheets. The simple forms of the whistler discussion of the reconnection layer suggest that these flows might approach $M^A_{\|,e} \simeq 43$ [*Shay et al.*, 1998], although two-fluid codes [*Ma and Bhattacharjee*, 1996] and particle-particle and hybrid codes [*Shay et al.*, 2001; *Hesse et al.*, 2001] suggest limits of $M^{A,\infty}_{\|,e} < 3$ for such flows in self-consistent evolutions; these theoretical/simulation limits are usually stated in units of the asymptotic Alfvén speed rather than the local Alfvén speed. The isolated temporal occurrence of these supra-Alfvénic electron flows is best seen in Figure 9 where the electron parallel heat flux, $q_{\|,e}$, and the asymptotic electron parallel Alfvén Mach number, $M^{A,\infty}_{e,\|}$, are plotted versus time for the interval 0630–0715 UT. The large electron parallel Mach number flows are usually seen on the gradients of magnetic intensity (not shown) when they are detected rather than at the local minima in the magnetic field strength. This is consistent with being near the separatrix boundaries of the nonideal MHD models of the reconnection layer (that include the ambipolar physics in the generalized Ohm's law). This conclusion is reinforced by the strong association of these flows with enhancements in the heat flux, which have previously been

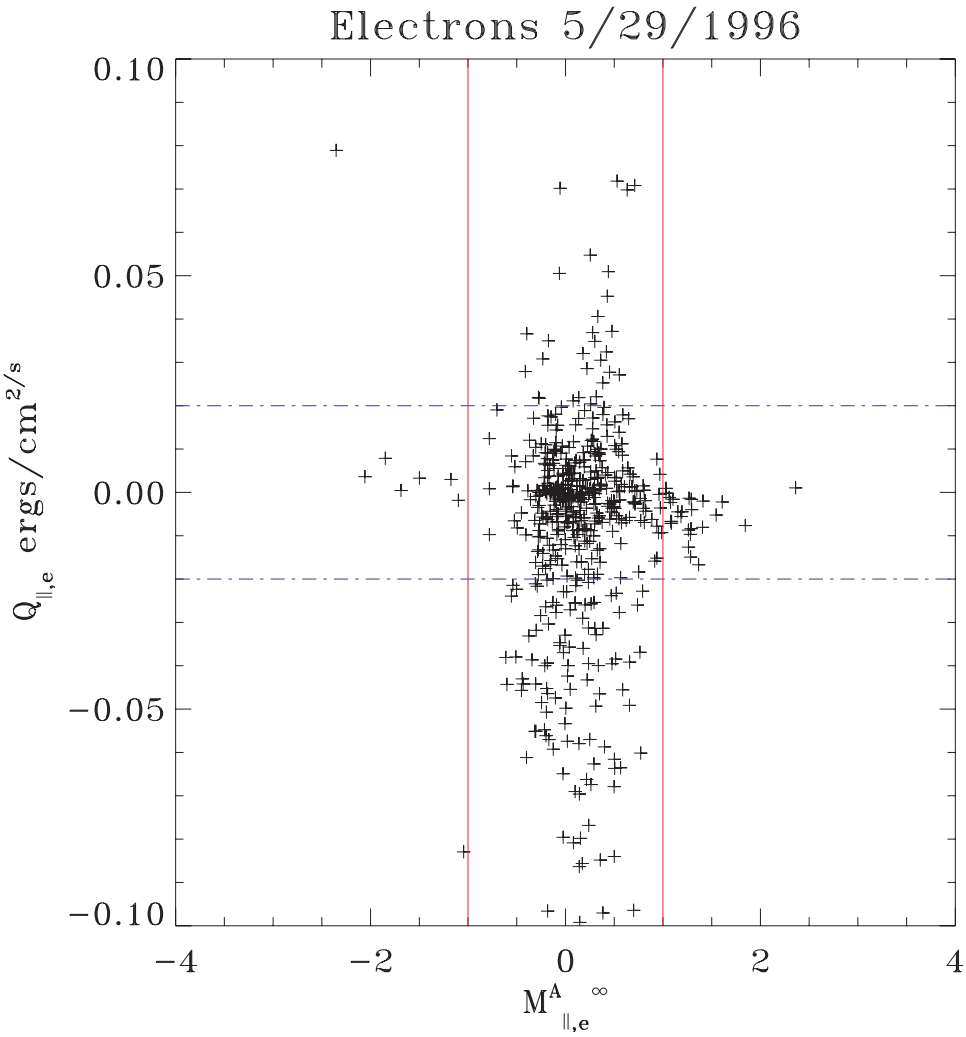

Figure 10. Coordination of $M^{A,\infty}_{e,\|}$ and $q_{e,\|}$. Asymptotic Mach numbers are computed with $V_A^{\infty} = 295$ km/s. Examples of coordinated $|M^{A,\infty}_{e,\|}| > 1$ and large $|q_{e,\|}| > 0.02$ are very rare compared to either large parallel Mach numbers or large heat flows alone.

interpreted [*Sonnerup et al.*, 1981; *Scudder et al.*, 1984] as a signature of the separatrix crossing. From Figure 9, the close association of enhancements in $|q_{\|,e}|$ and $|M^{A}_{e,\|}| > 1$ can be seen. That these layers are statistically dispersed can be seen in Figure 10, where a point is plotted at the coordinates $(M^{A,\infty}_{e,\|}, q_{e,\|})$ for each 4.6 s plasma spectrum. In Figure 10 the electron Mach numbers have been scaled by an assumed asymptotic Alfvén speed, based on the data seen when on the most sunward side of the layer. Figure 10 shows that supra-Alfvénic parallel Mach numbers for electrons are statistically disjoint from intervals with large conduction flux. If they were precisely spatially collocated, these extreme values would be found on lines with angles to the horizontal of other than (0°, 90°, 180°, 270°). Accordingly, the large electron parallel Alfvén Mach numbers cannot be artifacts of highly skewed distributions with these phase offsets; such a possibility could occur in slightly uncalibrated detectors. The time domain pictures illustrate that the heat flux layers and the high parallel Mach number intervals are often juxtaposed. Figure 10 also shows that when asymptotic estimates of the $M^{A,\infty}_{e,\|}$ are made that they, like the recent simulations, are bounded to be less than ~3.

5. Pressure Gradient Drifts

[47] If the electron pressure force explains the parallel electric field as suggested by Figures 5 and 6, then the component of this force perpendicular to **B** is significant (cf. inset Figure 6b), and there should be a signature in the average fluid motion of the electrons that would correspond to the electron fluid executing a superposition of electric and pressure gradient drifts. The three-dimensional electric and magnetic field measurements determine the electric drift:

$$\mathbf{U}_E = c\frac{\mathbf{E}\times\mathbf{B}}{B^2}, \tag{5}$$

while the pressure gradient drift for the electrons is expected to be given by

$$\mathbf{U}_{\nabla} = c\frac{-\nabla\cdot P_e}{en_eB^2}\times\mathbf{B}. \tag{6}$$

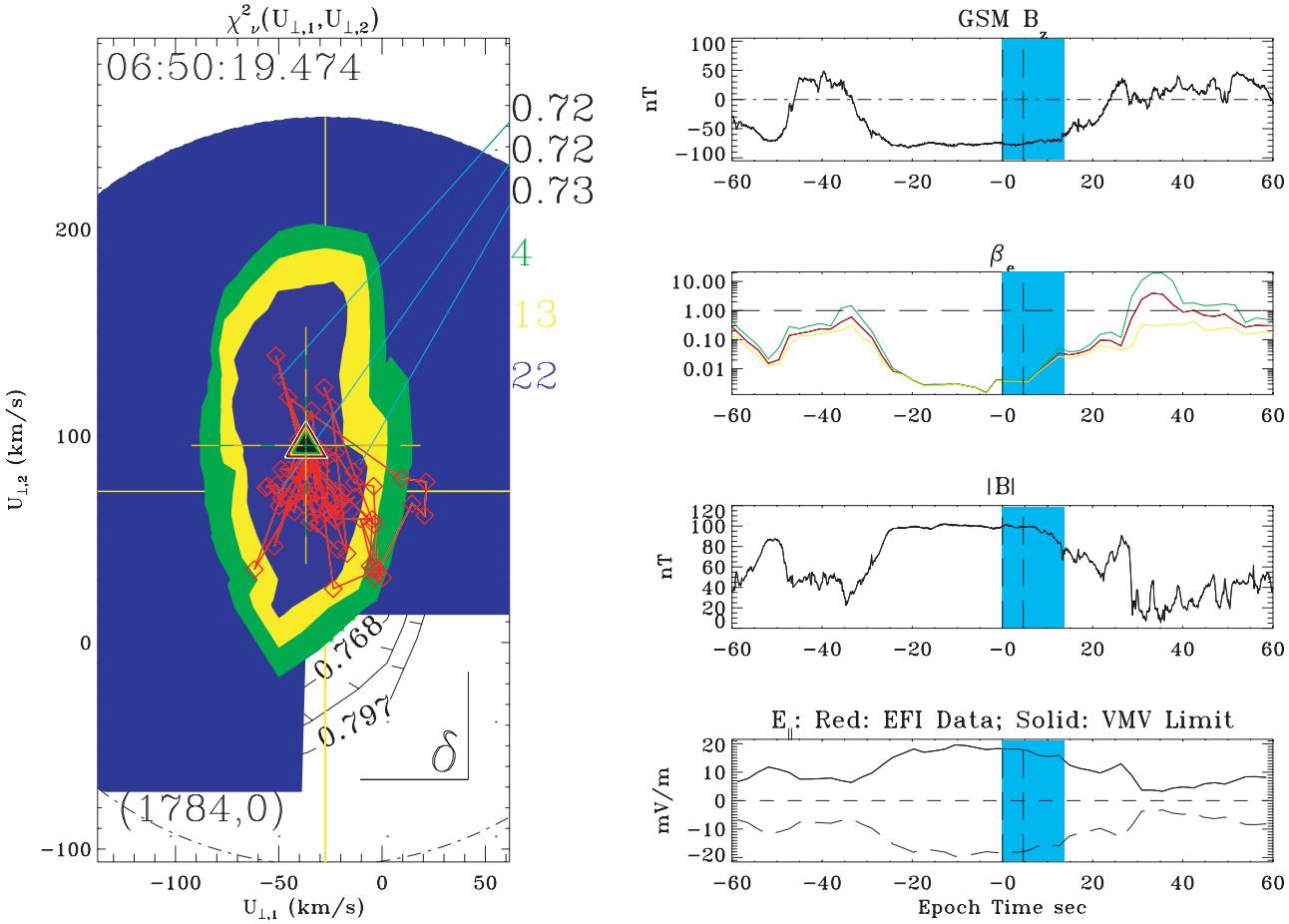

Figure 11. $\chi^2_\nu(\mathbf{U}_{\perp,e})$ surface using electron data collected between 0650:19.474 and 0650:23.804 UT for estimating likely electron $\mathbf{U}_{\perp,e}$ within gyrotropic approximation from data collected over 4.6 s. Numbers along right-hand side of contour bounding rectangle indicate the minimum χ^2_ν achieved (black) and in colors the percent of $\mathbf{E} \times \mathbf{B}$ estimates outside of green, yellow, or blue confidence intervals for the fit. Higher time resolution context for data in left-hand column made available in the right-hand column of plots. Bulk velocity comparison analyzed was acquired in a very low β_e regime away from current sheet. No $E_{\|} \neq 0$ data were certified by the stringent screening requirements discussed in Appendix A. While the Vasyliunas limit is significant, it implies an upper bound for the gradient drift that is not contradicted with the electron and **E** and **B** data. At virtually all levels of confidence the electron drift is indistinguishable from the $\mathbf{E} \times \mathbf{B}$ drift as suggested by nearly all the orange dots being inside the lowest confidence interval for the electron cross-field velocity.

Together these two drifts determine the electron fluid's motion in leading order as can be seen by taking the cross product of the electron momentum equation with **B** and neglecting DC and time-dependent inertial terms. Thus in leading order the electron fluid motion across the magnetic field is given by

$$\mathbf{U}_{e,\perp} \simeq \mathbf{U}_E + \mathbf{U}_\nabla \tag{7}$$

while the electric and magnetic field experiments determine $\mathbf{U}_E$ alone.

[48] Unless the pressure gradients are substantial, the pressure drift is usually small; such is the case in the solar wind, for example, where the ambipolar electric field is 10^{-7} the electric field associated with the unipolar term. However, our opening arguments concerning the scaling of $E_{\|}$ in our magnetopause layer imply that the pressure correction cannot be small while retaining the ρ_s scaling of the detected parallel electric fields.

[49] We proceed to test the idea that significant ambipolar $E_{\|}$ requires cross-field pressure gradient drifts of the electrons. To test the idea that pressure gradient drifts could cause discrepancies between the electron fluid's cross-field velocity, $\mathbf{U}_{\perp,e}$, and the $\mathbf{U}_E$ velocity, we have designed a format (introduced in Figure 11) that allows the reader to assess the degree of agreement between these two observables.

[50] Beyond the electric drift the electron cross-field drift would include the ambipolar electric field's contribution, which has a size

$$|\,\mathbf{E}_{\perp,ambi}\,| = E_{VMV} \sin\Psi,$$

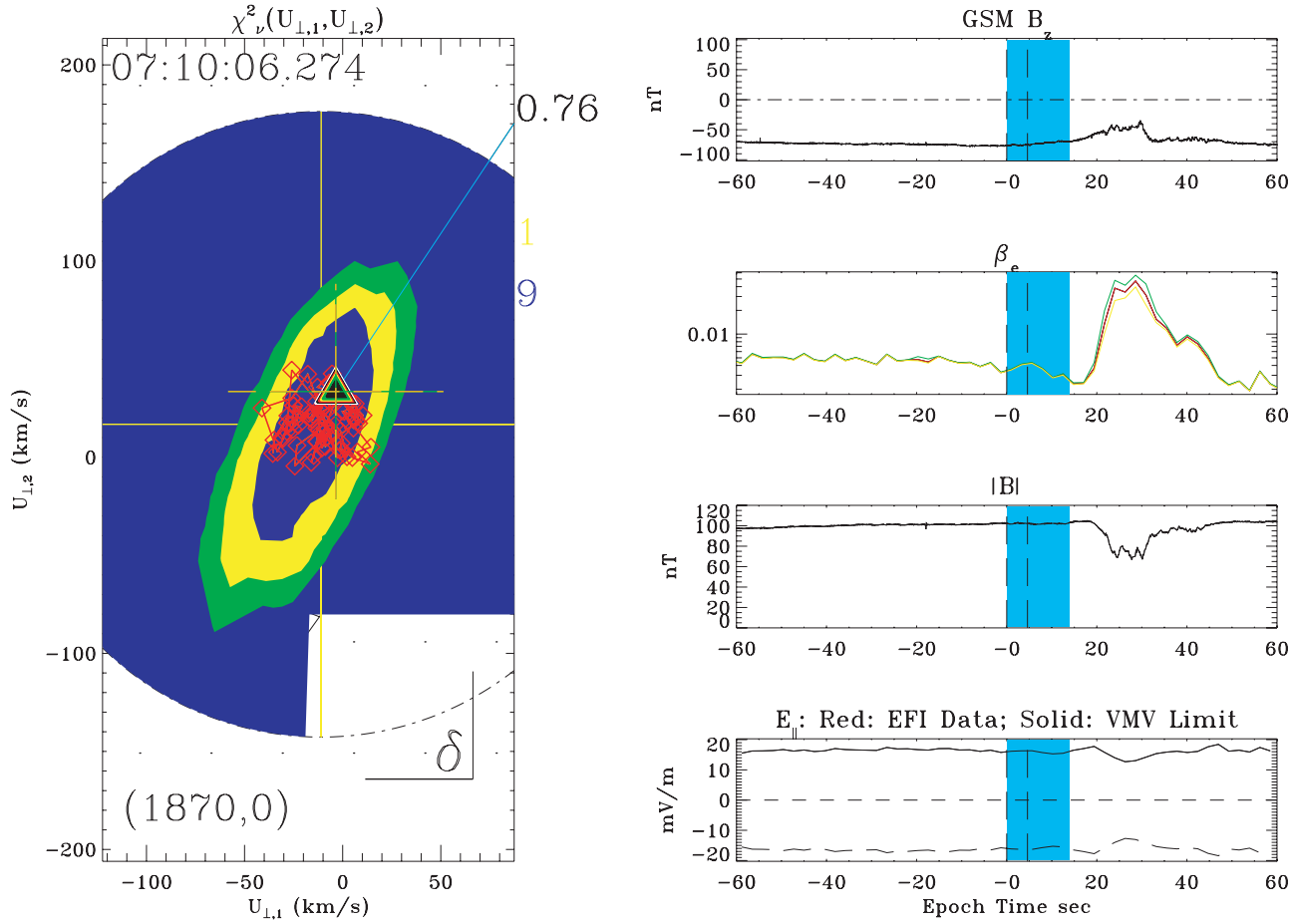

Figure 12. $\chi^2_\nu(\mathbf{U}_{\perp,e})$ surface using electron data collected between 0710:06.274 and 0710:10.604 UT. The data are consistent with no measurable pressure gradient drift.

which, in turn, simplifies to

$$| \mathbf{E}_{\perp,ambi} | = E_{VMV}\sqrt{1-\left(\frac{E_{\|}}{E_{VMV}}\right)^2}. \tag{8}$$

The implied speed of the pressure gradient drift is thus

$$\mathbf{U}_{\nabla} \simeq C_s\sqrt{1-\left(\frac{E_{\|}}{E_{VMV}}\right)^2}, \tag{9}$$

where C_s is the isothermal ion sound speed defined above with both species temperatures. The reported parallel electric fields in Figures 5 and 6 have been used in equation (9) together with equation (2b) to determine the expected difference between the total electron cross-field bulk motion, $\mathbf{U}_{\perp,\,e}$, and the electric drift, $\mathbf{U}_E$, determined by the magnetometer and electric field instruments. Figure 6c summarizes the distribution frequency of the pressure gradient drifts, $|\mathbf{U}_{\nabla}|$, suggested by the observed parallel electric fields and the contemporaneous Vasyliunas limits (using locally observed values of T_e and $\mathbf{B}$).

[51] While the spatial locales of detected $E_{\|}$ are not uniformly distributed in space, the size of the expected drift can be seen from equation (9) to be determined by the variability of the electron and ion temperature and Ψ throughout the interval. Although Ψ is variable and only precisely known when $E_{\|}$ is certified, the temperature does not vary greatly, so that for order of magnitudes this figure suggests 100–200 km s^{-1} might be the approximate maximum size of disagreements between the electric drift and the electron fluid's total drift. In any case knowledge of E_{VMV} and $|\mathbf{B}|$ places an important theoretical upper bound on the drift speeds that should be expected:

$$| \mathbf{U}_{\nabla} | \leq c\frac{E_{VMV}}{| \mathbf{B} |}. \tag{10}$$

As the magnetic intensity and E_{VMV} are more widely inferred than precise perpendicular drift speeds (that depend on certifying $E_{\|}$), equation (10) can be used to provide a more accessible bound on the possible pressure gradient drifts that might be expected. Our approach in the next five examples (Figures 11–15) is to contrast the electric drift with the best determinations of the electron fluid's perpendicular velocity, to ascertain if (1) they are operationally and defensibly distinguishable and (2) whether any such separations are appropriately bounded by the above inequality implied by equation (10). We first show two examples (one before and the other after the separator traversal) where the pressure

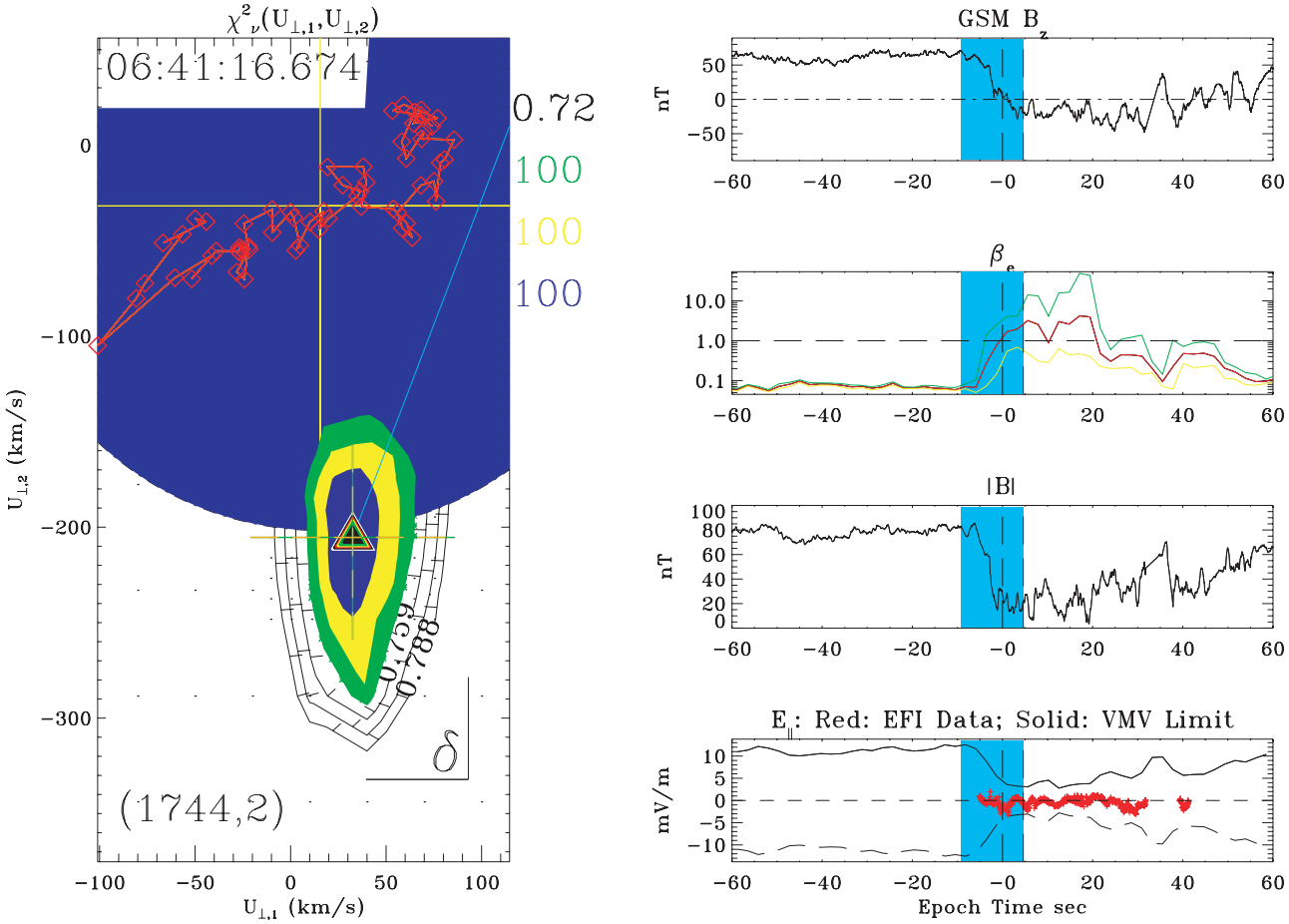

Figure 13. Interval when pressure gradient drifts of order 200 km s^{-1} are detected. Note that the measurements unlike those in Figures 11 and 12 straddle the current sheet crossing and occur at $\beta_e \simeq 1$. Same format as Figures 11 and 12. Yellow cross hairs of purple circle indicate average $\mathbf{E} \times \mathbf{B}$ drift for this interval. Note that extremities of purple circle overlap confidence intervals of the electron flow velocity, consistent with there being a vector solution, $\mathbf{\Gamma}$, to the equation $U_{\perp,e} = c\frac{\mathbf{E}\times\mathbf{B}}{B^2} + \mathbf{\Gamma}$, subject to the inequality $|\mathbf{\Gamma}| \leq c\frac{E_{VMV}}{B}$. The vector $\mathbf{\Gamma}$ determines the perpendicular part of $-\nabla \cdot P_e$.

gradient drift is so small (Figures 11 and 12) as to be consistent with zero considering measurement uncertainties; we then contrast these with three examples (Figures 13–15) where the pressure gradient drift has clearly been detected.

[52] The electron flow velocity at highest time resolution (4.6 s) is determined assuming that the electrons remain gyrotropic. $\mathbf{U}_{\perp,e}$ is determined by minimizing a chi-square function that is mathematically zero when the observer is moving with the optimal cross-field velocity so that the electron distribution function is most nearly cylindrically symmetric about **B**. In using this procedure, there is no assumption about the energy dependence of the velocity distribution being inventoried. The quality of the fit is measured by the so-called reduced χ^2_ν that determines the mean value of the departures of the data from the model in units of the expected random error. $\chi^2_\nu \simeq O(1)1$ are usually acceptable, will those much larger than unity imply an operational inconsistency with one or more premises under which the fit has been attempted.

[53] The χ^2_ν is a nonlinear function of the two unknown components of $\mathbf{U}_{\perp,e}$, which are in the plane perpendicular to **B**. Thus $\chi^2_\nu(\mathbf{U}_{\perp,e})$ is a surface whose global minimum is sought by finding the optimal $\mathbf{U}_{\perp,e}$ at the global minimum value. The two coordinates of $\mathbf{U}_{\perp,e}$ that are perpendicular to the average direction of **B** are referred to as ($U_{\perp,1}$, $U_{\perp,2}$). These basis directions, corresponding to (1, 0) and (0, 1) are dynamically determined by the average magnetic field direction during the data acquisition: One basis direction, $\mathbf{U}_{\perp,1}$, is parallel to ($-\langle B_y\rangle$, $\langle B_x\rangle$, 0), and the other, $\mathbf{U}_{\perp,2}$, is determined by a cross product of this direction with the mean magnetic field direction.

[54] In the left-hand column of Figure 11 the $\mathbf{U}_{\perp,e}$ fit plane topography of the χ^2_ν surface is contoured and color coded to indicate the equivalent confidence domains where $\mathbf{U}_{\perp,e}$ is suggested to lie, determined at the 68%, 95%, and 99.9% confidence levels using blue, yellow, and green filling the interior of the bounding contour. The perpendicular flow vectors consistent with 1σ confidence intervals are those within the blue-colored contour. At 68% confidence level all points within the blue region are operationally indistinguishable (Some note should be taken that it is the electron bulk velocity that is being determined from a velocity distribution that is much broader in speeds than an ion distribution. Hence the uncertainties are larger than

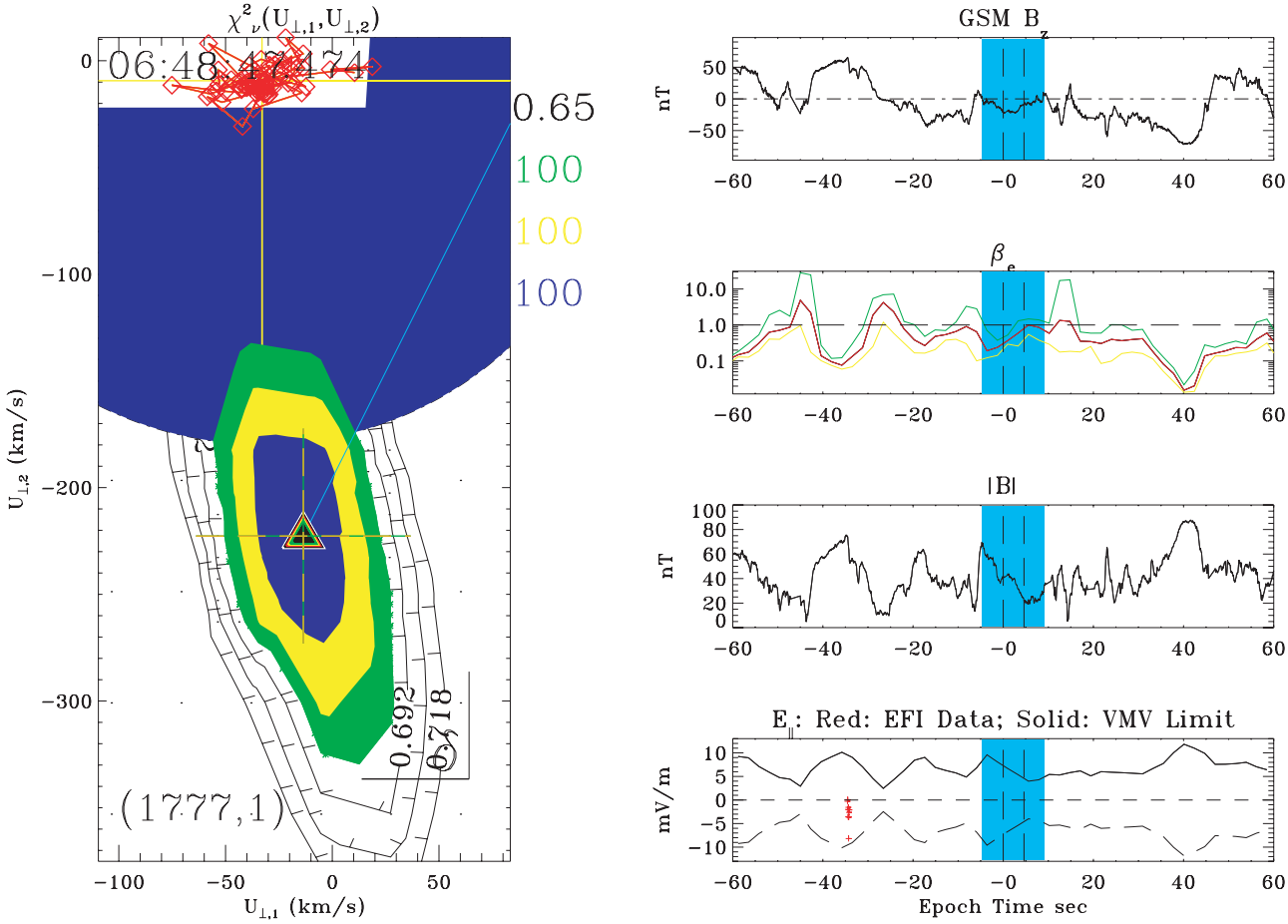

Figure 14. Additional example where significant pressure gradient drift inferred, consistent with the ρ_s bound indicated by the purple circle.

might be expected from the ion flow velocity determination, which in such current-carrying layers is not sufficient for our purposes; cf. Appendix A3). If a higher-confidence region is required, an augmented region of possible flow vectors must be included. This is done by forming the union of colored interiors from lower levels of confidence. Thus the highest (99.9%) level of confidence requires the union of blue-, yellow-, and green-shaded regions of possible locations for $\mathbf{U}_{\perp,e}$. Ideally, to show that two perpendicular velocities (e.g., $\mathbf{U}_E$ and $\mathbf{U}_{\perp,e}$) are clearly different requires that their respective confidence regions be disjoint as we show below in Figures 13–15. Confidence levels are constructed based on the sampled χ^2_ν surface [*Press et al.*, 1996], eschewing curvature formulae often used for linear least squares problems. This implies that the entire vicinity of the minimum has been sampled and searched. In fact, the entire rectangular box of extent $[\pm V_A]$ in both directions about the 13.8 s bulk speed for the electrons is searched for the optimal $\mathbf{U}_{\perp,e}$ reported here.

[55] The location of the numerical minimum of χ^2_ν sampled is indicated with a multicolored Δ symbol connected to a black number on the right vertical side of the contoured surface. The black call-out is the value of reduced χ^2_ν at the global minimum, being 0.72 in the example of Figure 11. Since the electric drift, $c\frac{\mathbf{E}\times\mathbf{B}}{B^2}$, only has components in this plane, the individual determinations of the electric drift velocity (which can be available up to 40 Hz) have been overplotted on this χ^2_ν surface as an orange connect-a-dot locus in Figures 11–15. There are usually many electric drift determinations available during the 4.3 s necessary to collect the plasma information used to determine the fit for $\mathbf{U}_{\perp,e}$. The colored numbers on the right-hand border of the contour plot indicate the percentage of $\mathbf{E} \times \mathbf{B}$ estimates that are outside the corresponding color's domain of confidence: blue, the percentage outside the 68% confidence interval; yellow, the percentage outside the 95% confidence interval; and green, the percentage outside the 99.9% confidence interval. The aliasing interval for the fit illustrated by the χ^2_ν surface is 4.6 s, and this time interval is indicated between the vertical dashed lines in each of the context figures in the right-hand column of Figures 11–15.

[56] The physical significance of Figure 11 may now be inventoried. Nearly all of the $\mathbf{E} \times \mathbf{B}$ estimates for the interval used by Hydra to determine the cross-field flow via the fitting procedure just described are within the 68% confidence interval for determining $\mathbf{U}_\perp$. Data of this kind are clearly consistent with no well-defined pressure gradient drift, even though a mathematically nonzero drift could be computed if only one Hydra flow vector was (incorrectly) assumed to characterize the electron measurements. When the errors of each observable is considered, as well as the

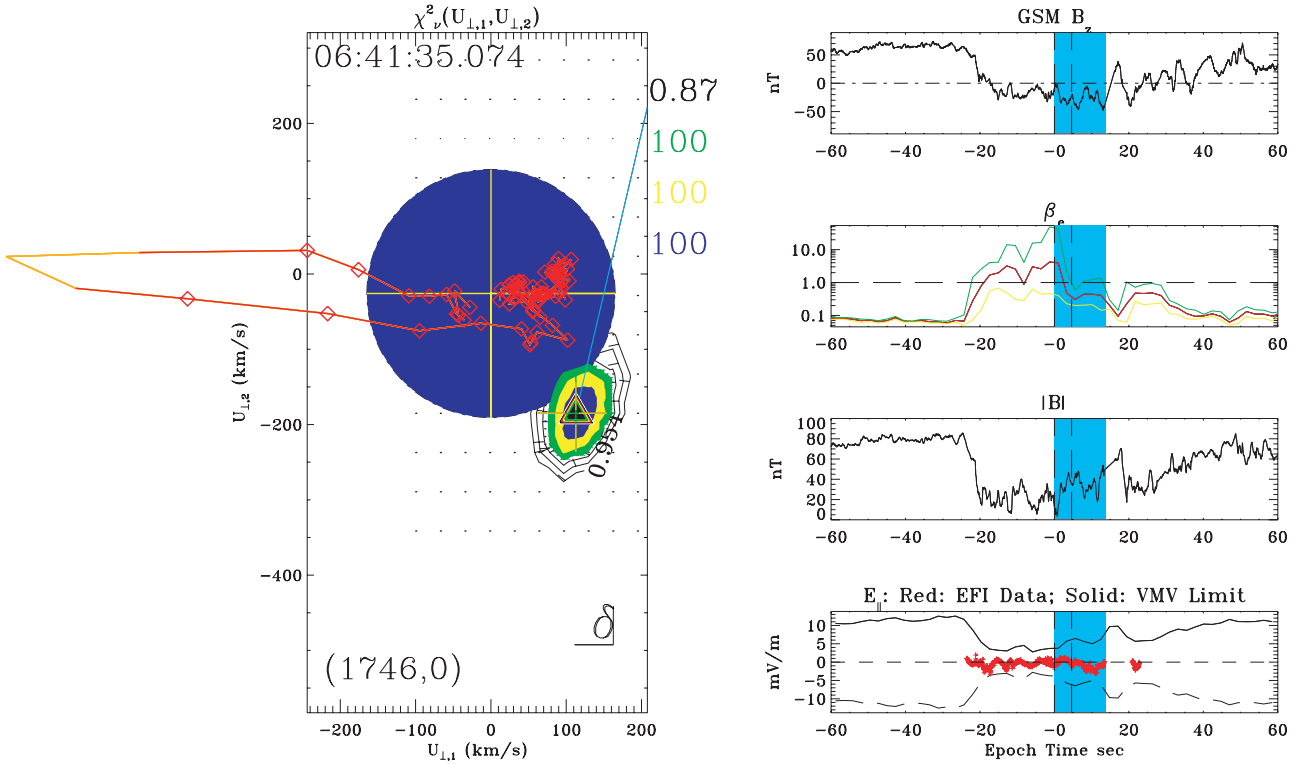

Figure 15. Strong pressure gradient drifts implied by the separation of the mean electric drift indicated by the intersection of the yellow cross hairs and the electron cross-field drift indicated by the multicolored Δ in the blue confidence interval.

underlying variance of the **E** × **B** determinations, a null result is the only defensible conclusion.

[57] The χ^2_ν is also acceptably low. This is an example where the pressure gradient correction is empirically not warranted. From the context plots of the right-hand column, these data were acquired in steady, strong fields in excess of 90 nT in a regime of very low $\beta_e \simeq 0.05$. In this regime the thermal electron gyroradius is 0.2 of the electron inertial length and 0.005 of the ion inertial length; such a regime is not conducive to electron Finite Larmor Radius (FLR) corrections even if the mechanical scales of this region were at the electron skin depth.

[58] To complete the format of these pictures, we now describe our procedure using the **E** × **B** data and E_{VMV} to infer the neighborhood of the **E** × **B** measurements where the electron cross-field drift should be found to support the ambipolar explanation for the newly certified $E_{\|}$ measurements being reported here. We average the **E** × **B** vectors in this plane and center at these coordinates a purple circle of radius $|\mathbf{U}_\nabla| = c\frac{E_{VMV}}{|\mathbf{B}|}$. This circle is laid down prior to contouring the χ^2_ν surface with its colored confidence regions. As may be seen in Figure 11, this circle is nearly concentric with the confidence region for the fit electron cross-field flows. The yellow "cross hairs" superposed on this circle identify the mean coordinate of **E** × **B** selected. In the presence of perceptible gradient drifts, the purple circle's center will not be enclosed within the 99.9% confidence regions of the electron cross-field determination. If the ambipolar hypothesis is supported in the presence of pressure gradient drifts, the confidence intervals for finding $\mathbf{U}_{\perp,e}$ should partially overlap the purple circle. The vector connecting the center of the purple circle and the lowest point in χ^2_ν should have a length less than or equal to the radius of the purple circle in order that the Hydra, MFE, and EFI measurements be simultaneously consistent with equation (10) and our ambipolar identification of the cause of the certified $E_{\|}$ summarized in Figure 6.

[59] Data collected after the separator crossing are used in Figure 12 to demonstrate another "no pressure gradient" signature. The χ^2_ν is 0.76 and hence acceptable for interpreting the minimum as a perpendicular flow speed for the electrons. All but 1% of the **E** × **B** determinations are inside the 95% confidence contour, and none are outside the 99.9% contour for the electron drift speed.

[60] (Although Polar does not enter the undisturbed magnetosheath frequently, it has done so, and on such passes we have compared the electron fluid cross-field flows with those implied by **E** × **B**. An interval when Polar punched out into the solar wind is illustrated in Appendix A3 (Figure A7), to show that there is routine agreement between $\mathbf{U}_{\perp,e}$ and **E** × **B** in the magnetosheath and even in the solar wind.)

[61] An interval where the pressure gradient is suggested to be important is illustrated in Figure 13, using our by standard format. The electric drift (orange locus) of **E** × **B** estimates are totally inconsistent with the suggested 99.9% confidence interval (indicated by the union of blue-, yellow-, and green-filled contours) for the perpendicular bulk flow of the electrons. All the electric drift estimates are well outside the highest confidence interval for localizing the electron's total cross-field drift. Estimating the **E** × **B** drift error with $\delta E = 0.5$ mV m^{-1} in a 20 nT field and 50 km mean **E** × **B**

flows, the uncertainties are of order 25 km s^{-1} (Thus the $\mathbf{E} \times \mathbf{B}$ estimates are disjoint from the 99.9% confidence intervals in the electrons even after this uncertainty is considered). The normalized $\chi^2_\nu \simeq 0.72$ for the "best fit" $\mathbf{U}_{\perp,e}$ is acceptably ranked, so that the identification of the minimum of the χ^2_ν surface with a physical cross-field electron flow is consistent with the gyrotropic model being fit. Even though there is some variation in the magnetic field in evidence in the detail context plot, the low value of the minimum of χ^2_ν suggests that the data and its errors are not too sensitive to their having been acquired with the ±10 nT variation of B_z during the data collection interval. The maximum pressure gradient drift allowed by equation (10) is indicated by the radius of the purple circle centered on the average electric drift position. This purple circle overlaps the highly likely positions indicated for the best fit cross-field velocity of the electron gas for this period.

[62] This is a period as indicated in the detail data plotted in the right-hand column when $E_{||}$ has been certified. However, as indicated in the fourth right-hand panel, these parallel electric fields are well below the maximum possible under the Vasyliunas premise; this implies that a considerable, if not dominant, part of the bound in equation (10) would be expected to show up in the cross-field drift. Consistent with this circumstance, it is of interest to note that the purple circle does not need its maximum radial extent from the average electric drift location to overlap the expected regime of the electron flow.

[63] As the context plots indicate, the regime of these observations are near the GSM B_Z reversal, are in a $\beta_e \simeq 1-3$ plasma, (a regime where the thermal electron gyroradius and the electron inertial length are essentially the same), and in a region where the parallel electric fields were observed (lower context panel in red). This is a regime where electron fluid FLR corrections could be anticipated. If the current sheet structure in this example were at the electron skin depth scale, the thermal electrons are marginally magnetized. That the normalized χ^2_ν is so acceptably ranked is an indirect argument that the spatial scales of the current layer are not so steep that a gyrotropic parameterization of the distribution would be disrupted.

[64] We thus conclude that Figure 13 illustrates the detection of an electron pressure divergence drift of magnitude 150–200 km s^{-1} with an extremely high (99.9%) level of confidence. Of particular importance is the demonstration that there is a vanishingly small chance that this difference is consistent with zero pressure gradient drift. This circumstance should be contrasted with the same considerations in Figures 11 and 12, where the chance for zero drift is almost certain, given the exhibited variability and the demonstrated uncertainties.

[65] Additional evidence for pressure gradient drifts of approximately the correct size expected by the ambipolar hypothesis is presented in Figure 14 for the interval starting at 0648:47 UT. Disjoint average $\langle \mathbf{U}_E \rangle$ and $\langle \mathbf{U}_{\perp,e} \rangle$ are clearly illustrated, with all $\mathbf{U}_E(t)$ being outside the most stringent confidence intervals for $\mathbf{U}_{\perp,e}$. The minimum $\chi^2_\nu = 0.65$ clearly demonstrates that the fit is consistent with the gyrotropic presumption and that the fit drifts are viable as physical drift attributes for the electrons at this time. The displacement of the electron fluid drift from the electric drift estimates is suitably "linked" by the purple circle of radius determined by equation (10). We conclude that this example is nearly incontrovertible proof of detection of the pressure gradient drift of 250 km s^{-1} at the 99.9% level of confidence. From our context plots in the right-hand panel we see that this example occurs in a $\beta_e \simeq 1$ regime near to, but not at, the GSM reversal of B_z.

[66] Another example where pressure gradient drifts are strongly suggested where parallel electric fields are also measured is illustrated in Figure 15. This interval occurs in a region of changing conditions; in spite of the changes in the magnetic field the $\chi^2_\nu = 0.87$ is still acceptable for interpreting the location of minimum χ^2_ν as the electron drift velocity. A pressure gradient drift of ~210 km s^{-1} is inferred from the Hydra, EFI, and MFE comparisons, a result clearly less than the maximum drift indicated by local parameters and equation (10) indicated by the purple circle. Notice, here too, that $E_{||}$ has been certified in this interval, but it is a small fraction of the local value of E_{VMV} indicated by the black traces in the fourth right-hand panel of Figure 15.

6. Agyrotropy, β_e, and $L \simeq \frac{c}{\omega_{pe}}$

[67] Our method for determining high time resolution (4.6 s) cross-field flow velocities is designed to answer two questions: (1) Are the electrons gyrotropic and (2) if so, with what transverse bulk velocity must an observer move who perceives the observed electron fluxes as gyrotropic? Positing gyrotropy is (1) a precondition for (2) determining a cross-field flow velocity. The examples shown above in Figures 11–15 have low χ^2_ν; because these examples met the test of gyrotropy, the second level diagnostic was appropriately associated with the electron fluid's cross-field flow velocity and used to compare with the $\mathbf{E} \times \mathbf{B}$ drift velocities. However, a high value of χ^2_ν vacates the second step of the logic, making the value associated with the minimum in χ^2_ν a numerical set of coordinates without a physical interpretation. A fit "solution" that after searching the space to decrease χ^2_ν cannot reduce it to an acceptably ranked level becomes a measure of the violation of postulate (1) made to perform the fit (Being a nonlinear fit, it is important to reiterate that we have canvassed the fit space, rather than performing a gradient search; gradient searches are well known for becoming "lost" in local minimaxes that are possible in nonlinear minimization problems. The minimum χ^2_ν reported here is the global minimum of the surface that has been tabulated on a mesh with a resolution comparable to our minimum expected resolution with this detector as shown by model simulations). We now use the temporal variation of the minimum $\chi^2_\nu(t)$ found to provide information about the possibility that the electron distributions themselves have been disrupted.

[68] The first remarkable fact of this study is that the mode χ^2_ν is 1.12, even after attempting to fit all 704 spectra in this interval. Accordingly, periods of possible interest for failing the gyrotropy precondition are those where $\chi^2_\nu \gg 1.12$. Sometimes the minimum of χ^2_ν is unacceptably "ranked" [*Press et al.*, 1996] during a 4.33 s plasma data acquisition interval. A possible hidden reason for not having an acceptably ranked χ^2_ν could be that the magnetic field was rapidly varying during the time of the data collection, so that high χ^2_ν would indicate discordance with a cylindrical and time-independent model for the electron velocity

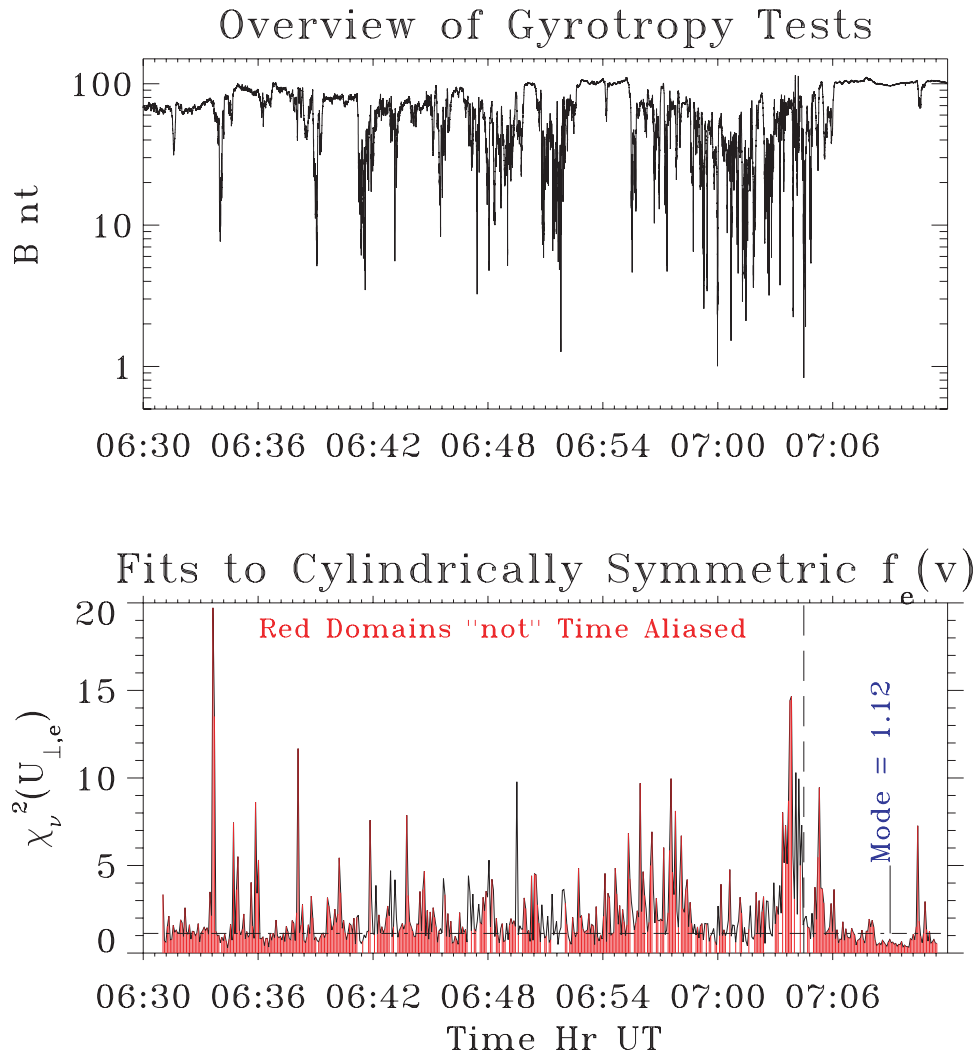

Figure 16. Variation with time of magnitude of **B** in the first panel and the normalized χ^2_ν (second panel) for determining electron cross-field bulk drift at 4.3-s resolution. Vertical black dashed line in first panel indicates the location of the weakest magnetic depression illustrated in Figure 3. Red vertical lines highlight portions of the $\chi^2_\nu(t)$ curve where time variations of the orientation of **B** make the direct interpretation of high χ^2_ν as agyrotropy (nongyrotropy) a distinct possibility.

distribution over the 4.3 s necessary to acquire the raw data. This type of aliasing is in principle convolved into all plasma measurements that are slow compared to microscopic time scales. To guard against an inappropriate inference of agyrotropy, we have screened out fit intervals for possibly higher-frequency variations of magnetic field direction during the 4.33 s. Using 54 Hz samples, we have inventoried the Pythagorean variance of **B** as a possible cause of apparent deviations from gyrotropy. The Pythagorean variance was used to determine an RMS angle of the field's variation during the 4.3 s of electron flux acquisition. If this RMS angle was more than half of Hydra's 7° sensor full width angular response, we have indicated below that these intervals cannot have their high χ^2_ν attributed to FLR effects in the electrons.

[69] In Figure 16 we highlight in red portions of the envelope of $\chi^2_\nu(t)$ where time aliasing is "not" a factor. Intervals where high χ^2_ν are determined and supported by a red line to the χ^2_ν value require something beyond field volatility as indicated in the second panel of Figure 16. The high resolution magnetic intensity profile is displayed for context in the first panel of Figure 16. As seen in Figure 16, there remain episodic intervals of large χ^2_ν that are not readily attributable to simple time aliasing of an otherwise gyrotropic distribution function. Although the occurrence of high χ^2_ν is not correlated one for one with extreme magnetic field reductions, it should be remembered that the communication within this maze of thermal electrons with gyroradii as large as 10 times the scale structures detectable in **B** could easily lead to a lack of precise temporal localization between locales of weak fields and the precise locations where electrons are observed to be disrupted.

[70] A further organization of the large χ^2_ν population in this data set is afforded by Figure 17, where $\chi^2_\nu(\beta_e)$ as a function of the local value of the electron β_e is displayed. The first pattern of Figure 17 is to note that the highest values of χ^2_ν occur at $\beta_e > 1$, while equally noteworthy is that all the aliased estimates of χ^2_ν are primarily at the

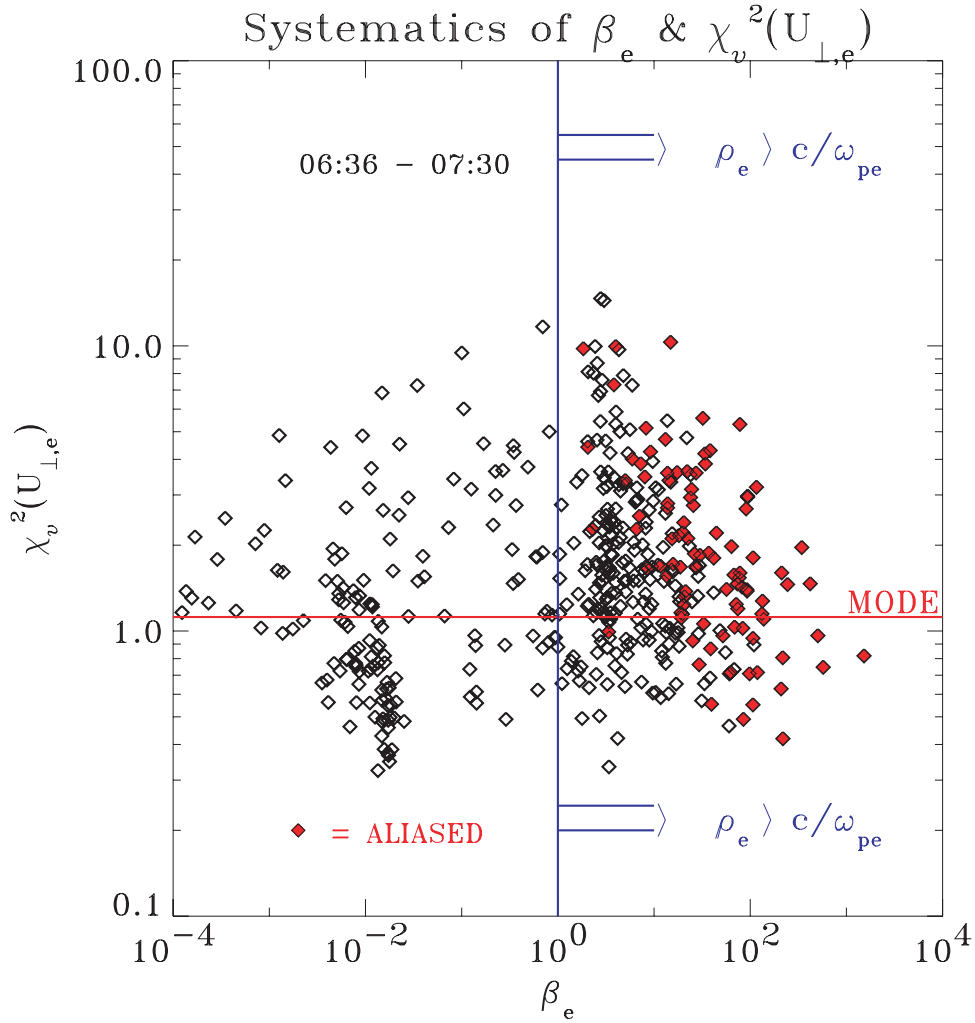

Figure 17. Black diamonds indicate the locations of all $\chi_\nu^2(\beta_e)$ regardless of the value of χ_ν^2 or the variability of the direction of **B**. Red-highlighted diamonds indicate spectra where magnetic variability shadows a simple interpretation of high χ_ν^2.

highest β_e's sampled. While there are $\chi_\nu^2 > 1.12$, across the range of β_e's sampled in this data set, the largest number of such large and high, unaliased χ_ν^2 are found at $\beta_e > 1$.

[71] Particularly interesting is that high χ_ν^2 spectra almost totally avoid the $m_e/M_p < \beta_e < 1$ interval that accompanies almost all the certified $E_{\|}$ certifications indicated in Figure 6f. This suggests that high beta regime that are also in short electron skin depth scale regions could be the cause for the large, unaliased χ_ν^2 estimates indicated in Figure 17. We will show in the sequel that electron skin depth scales are achieved in such layers and make this possibility a very strong candidate to explain the data.

[72] Theory [*Vasyliunas*, 1975] suggests there should be three layers as the separator is approached: (1) In an outer zone with scale lengths of the ion inertial length, the current layer is perceptible, and the electron fluid becomes uncoupled from the ion fluid, with the electrons still magnetized and "carrying" the magnetic field (In this region and all subsequent inner scales, **J** × **B** corrections to the generalized Ohm's law are important); (2) In the next innermost layer the electron pressure ridge continues to grow, so that the electrons while still magnetized will experience electric and pressure gradient drifts, all the while carrying magnetic fields in so-called electron magnetohydrodynamics (EMHD); this layer has the scale, ρ_s, associated with Vasyliunas's argument. In this region the electrons are magnetized even while electron FLR pressure gradient drifts are important; however, it is a regime where the electron thermal gyroradius is smaller than but not zero compared to the gradient scale lengths. In this regime our approach for getting comparisons between electric and electron drifts should have low χ_ν^2 while still indicating pressure gradient effects as in Figures 13–15; (3) On the innermost scale of the electron inertial length, there comes the regime where the electrons are most surely unmagnetized and on this scale the gyrotropic hypothesis could be expected to be falsified by the high minimum values of χ_ν^2 we have detected. We emphasize that the precise locales where the electrons should be seen as agyrotropic may be a considerable distance (indexed in electron skin depths) from the weak field structures that may shape their properties. It should also be emphasized that the canonical picture of

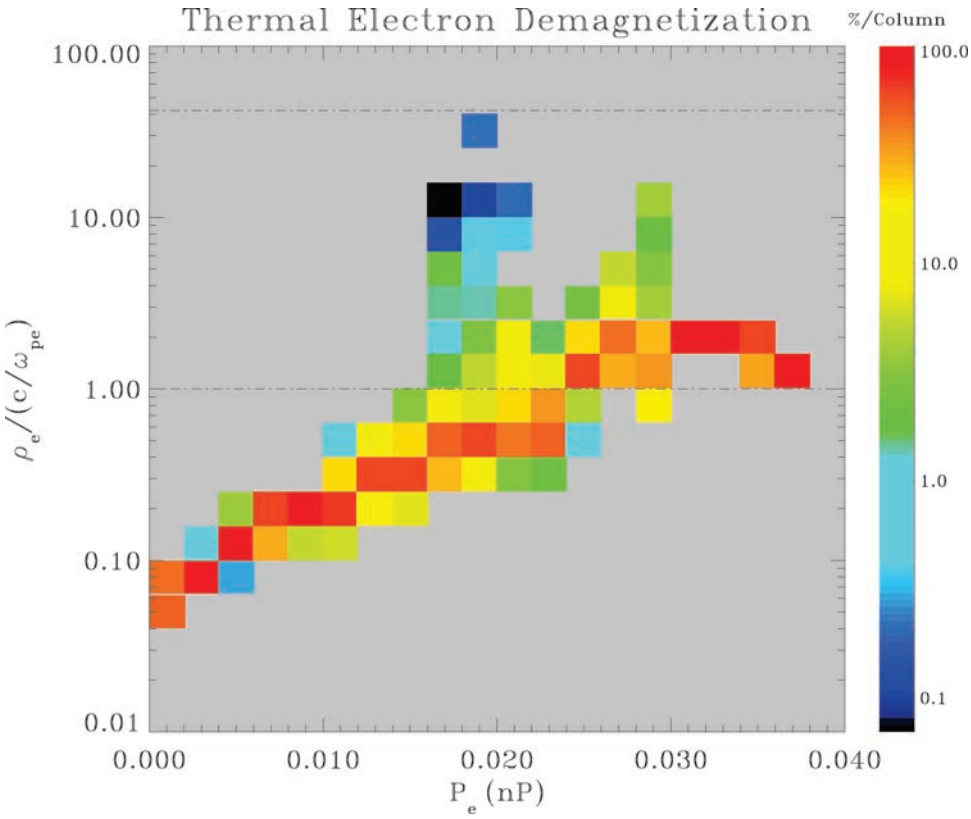

Figure 18. Observed dimensionless thermal electron gyroradius ($Y = \rho_e/(c/\omega_{pe})$ versus electron pressure ($X = P_e$), color coded by percent occurrence in fixed pressure intervals. The general trend is for the inertial length scaled electron gyroradius to increase as the observed electron pressure increases. Numerous examples exist with this scaled gyroradius above unity, especially at higher pressures.

collisionless reconnection leads to a time-independent view of the process that requires the electron gyro-mechanics to be disrupted in such a way that the pressure tensor has a time-averaged structure near the separator that is not diagonal in the local magnetic frame of reference; hence the velocity space pattern is thought to have a nongyrotropic imprint that is time independent. Although the Larmor period of the electrons is much too short for Hydra to capture gyro-phase bunching of electrons, there remains the possibility that the pattern of sampled $f_e(v, t)$ during the time of 4.3 s may have remnants of this time stationary departure from gyrotropy required by the collisionless theory of magnetic reconnection.

[73] A further aspect of the ambipolar mediated "flavor" of the collisionless magnetic reconnection hinges on generating dynamical circumstances where the departure from cylindrical symmetry in the electron pressure tensor, P_e, can persist in time, at least in a limited region around the separator [*Vasyliunas*, 1975]. Broken cylindrical symmetry of the electron pressure tensor around the magnetic field direction is referred to as the "agyrotropy" of the distribution. When not gyrotropic, electric fields along the separator and its vicinity arise from the ambipolar term. The tensorial character of $P_e(x, z)$ coupled with the divergence operator implies electric fields of the ambipolar type can be produced along the separator line along the **y** axis. In the simple 2-D pictures of reconnection the flow is stagnant at the separator so that the electric field tangential to the magnetopause along this separator line cannot be supplied near the separator by the unipolar term. The full divergence of the electron pressure can fill this void and supply the missing electric field components along the separator, especially in the absence of resistive emfs ($\eta \cdot \mathbf{J}$), a situation considered extremely relevant in space reconnection scenarios. In his review paper Vasyliunas makes the argument that the needed form for the electron pressure tensor is such that all three of its eigenvalues are distinct, and hence it is agyrotropic. This is especially true within one thermal electron gyroradius of the separator line.

[74] There is also a general association in Figure 16 of the increases in χ^2_ν, agyrotropy, with depressions in field strength, although the association is not one to one. If the scaling is correct, the electron gyroradii sampled at time t_1 do not only reflect the magnetic field strength in this locale but also the variation of **B** over the adjoining thermal gyroradius. One interpretation that we adopt is that the $\chi^2_\nu \simeq O(1)1.12$ reflects layers (1 or 2) above, where the electrons are decidedly magnetized; this leaves the unaliased high χ^2_ν regions as those inside the very high β_e current channel is surmised to have $\frac{c}{\omega_{pe}}$ scales, where the electrons would most assuredly become unmagnetized. We solidify this argument in the sequel.

[75] The large values of electron β_e that occur in this and immediately adjacent regions facilitate a necessary prerequisite for such asymmetric pressure tensors: thermal

gyroradii much larger than electron skin depths (anticipated as the limiting current channel widths in the reconnection layer). This may be seen since the electron gyroradius,

$$\rho_e = \beta_e^{\frac{1}{2}} c/\omega_{pe}, \tag{11}$$

can be strongly enhanced with the high values of β_e implied in Figure 6f. In the separator's vicinity the electron's Larmor radius significantly exceeds the electron inertial length by more than a factor of 25. At these high betas the electron gyroradius is within a factor of 2 of the ion inertial scale length, the overall scale of the currents that make up the Hall zone of the Chapman-Ferraro current layer. Clearly the gyroradius is not well approximated in such regimes by these simple formulas. Such large ratios clearly indicate that the guiding center ordering for the thermal electrons can seriously be disrupted if such ratios occur in electron inertial scale length regions expected at the current layer. In Figure 18 we have indicated the percentage distribution of the dimensionless thermal electron gyroradius, that is, $\beta_e^{\frac{1}{2}}$, as a function of local electron pressure. Each vertical column in Figure 18 is in a fixed pressure interval. The location of the boxes in the vertical direction depicts the populated dimensionless gyroradii, while their color indicates the percentage occupancy within that column at that dimensionless gyroradius. A clear pattern for the dimensionless gyroradius to go up with pressure is indicated, a result that is implied by the progression of the β_e lines in Figure 6. The new points in this format are (1) the frequency that the dimensionless electron thermal gyroradii exceed unity and (2) the pattern of this behavior with increasing electron pressure (and hence decreasing magnetic field pressure). In the sequel to this paper we demonstrate with superposed epoch spatial portraits that the regimes of large dimensionless thermal electron gyroradii occur in regions with scale lengths at the electron skin depth so that the trend of this picture does indeed imply the detection of strongly demagnetized electrons at the higher pressure and precisely those higher pressures where the ion perpendicular Alfvén Mach number is highest.

[76] We thus have documented for the first time a situation where the thermal electrons in these high β_e regimes at the separator are increasingly unmagnetized, and especially so in the highest β_e regimes. If, as in theory, the innermost spatial scale of the magnetic separator regime approaches the electron inertial length, then these high β_e electrons are clearly unmagnetized and capable of jumping "field lines," facilitating a change of magnetic topology in a collisionless way. Because the thermal electrons have the smallest gyroradii in the plasma, their mobility at this scale removes the conceptual possibility of labeling field lines by any well-defined set of occupants. It also removes the adiabatic style arguments that the electrons should remain cylindrically symmetric in such locales, completing the Vasyliunas picture of how collisionless magnetic reconnection is sustained. Within the diffusion region explored here, the external laminar MHD description in terms of "moving field lines" must be forsaken for a more complete description of the electromagnetic field in terms of the four-vector potential.

7. Summary

[77] This paper provides the first empirical evidence that delineates the process of collisionless magnetic reconnection within the nonideal MHD layers where it is occurring. Beyond the previous Walén tests for tangential stress balance that we have performed for this data at the magnetopause [*Scudder et al.*, 1999], we have in this paper introduced quantitative evidence for the: (1) first documented penetration of the three spatial scales nested about the separator expected from collisionless theory, with attendant Walén tests that have opposite slopes, (2) first detection of $E_{\|}$ at the magnetopause, (3) first quantitative and empirical argument that this parallel electric field is ambipolar in character, (4) first detection of the electron pressure ridge astride the magnetic depression at the separator, (5) first empirical detection of the reconnection rate with the sub-Alfvénic ion inflow, $M_{i,\perp}^{A} \simeq 0.1$, and local trans-Alfvénic outflow, $M_{i,\perp}^{A} \simeq 1.1-5$, (6) first empirical detection of supra-Alfvénic electron parallel Alfvén Mach numbers in excess of 5 in narrow sheets, (7) detection of heat flux sheets near, but not always in, superposition with, the supra-Alfvénic parallel electron bulk flows, (8) first evidence that pressure gradient scales are short enough within the magnetopause to provide observable ambipolar corrections to the electron fluid's unipolar electric drift, including experimental demonstration that the relative drifts between the electron fluid and the $\mathbf{E} \times \mathbf{B}$ drift are consistent with locally constrained ambipolar drift velocities, (9) first detection of departure from electron gyrotropy not only at the separator crossing but also in its vicinity, most usually where $\beta_e > 1$, (10) first reports of very large values of electron $\beta_e \simeq 680$ that imply the electron thermal gyroradius strongly exceeds the local electron inertial length in such regions and is within a factor of 2 of the ion inertial length near the separator, (11) first organization to show that poor examples of electron gyrotropy are associated with $\beta_e > 1$; if spatial scales are below the electron inertial length, or even close, then the thermal electrons, as a fluid, are unmagnetized, providing the ultimate nonideal MHD feature that permit collisionless reconnection to be understood; to provide closure on this argument and explanation of the strong correlation of agyrotropy with high electron $\beta_e > 1$, we must demonstrate in future work that the innermost spatial scales of this layer do asymptote to the local electron inertial length, and (12) first demonstration that the observations of $E_{\|}$ are almost exclusively found in regimes that satisfy $\frac{m_e}{M_p} < \beta_e < 1$, while the domain of large inferred departures from gyrotropy are most frequently a $\beta_e > 1$ circumstance; the incidence of certified $E_{\|}$ rather strictly satisfies this first inequality as would be expected for their being associated with the distinct ρ_s scale; this is true in spite of the fact that the typical magnetic field strength when $E_{\|}$ has been certified is noticeably smaller than the most frequently occurring or mean field strength encountered in the surveyed interval.

[78] The determination of a self-consistent geometry and the reconstruction of the spatial interrelationship of the time

sequence of diagnostic parameters of this encounter with the separator will be developed in future work.

Appendix A: Experimental Issues and Concerns

[79] Given the uniqueness of the results in this paper, we have made critical evaluations of all measurements, their sources of errors, and the assumptions made for derived parameters calculated from the engineering measurements. Where direct knowledge of the effects of assumptions and errors is not completely quantifiable, we revert to how well the measurements support one another and with applicable physics as a test of their validity. We believe that we have addressed all known sources of errors in the measurements and have found nothing that would invalidate our results. The following sections summarize our evaluations of the measurements.

A1. 54 Hz Magnetic Field Trace Reconstruction

[80] Two issues are relevant from the magnetometer data used in this study: the reconstruction of the 54 Hz B data that comes down in Hydra's telemetry and zero levels and offsets.

A1.1. Zero Levels and Offsets

[81] The primary concerns are those of drift of the zero level. The alignment of the sensors are maintained within 0.1° of the inertial reference frame by comparing with the Earth's field every orbit and taking a long-term average. The intersensor alignment is maintained by phase comparisons to better than 0.01°. The zero level in the spin plane was calculated by running averages over 15 spin periods and then adjusting for any difference between the old and new values by changing the old offset by no more than 10% of the difference and only changing values if the field was steady. The zero level along the spin axis was obtained by flipping the spin axis sensor into the spin plane for several orbits and averaging as with the usual spin plane sensors. The values obtained were independently checked in two ways: (1) by comparing the observed field in the solar wind on 4 May 1998 when Polar entered the solar wind with measurements made by permanent solar wind observatories and (2) by calculating the average spin axis field when the spin plane field was <2 nT. In each case the calculated zero level agreed with that expected to within 1 nT, and it was statistically consistent with no error within one standard deviation. Thus we have 95% confidence that our zero levels are within 2 nT of zero on 29 May 1996 even in a dynamically changing ambient field.

A1.2. 54 Hz Integrity Checks

[82] The high temporal resolution data reported in this paper comes from a telemetry stream that passes between MFE and the Hydra instrument on board the spacecraft. It is filtered within Hydra's onboard data processing unit and sampled down from 108 Hz and put into Hydra's telemetry stream for use in unpacking the Hydra plasma data. Only high resolution polar angles of **B** are returned in this manner by the Hydra telemetry stream. This reconstruction is the topic of the next section in this appendix. We have verified that our 54 Hz data stream filtered to 8 Hz agrees with the MFE reconstruction of **B** based on their independent telemetry. We also discovered some erroneous spikes in the high-speed sampling of **B** that have been reproduced by the MFE high data rate mode and subsequently fixed. Our 54 Hz data stream is edited for these spikes with a method and software approved by the MFE team. These spikes, attenuated by averaging, also survive in the 8 Hz magnetic field data; these have been removed on the basis of the anomalies detected in the 54 Hz data stream. Details of the onboard filtering and distribution of magnetometer data are available on the World Wide Web at http://www-ssc.igpp.ucla.edu/polar/DataFlow.html.

A1.3. 54 Hz Magnitude Reconstruction

[83] The normal full magnetic field records (B_x, B_y, B_z) of this day are available through the MFE telemetry stream at a repetition rate of 8 Hz. Each component reading of **B** at 8 Hz represents a decimation of the output of an antialiasing filter of data acquired on board the spacecraft at a much higher frequency. This filter caused this 8 Hz data to lag abrupt changes in the field's magnitude or direction. 54 Hz polar angles of **B** are transmitted in Hydra's telemetry. We have asked ourselves what set of magnitudes should be associated with our 54 Hz angles to be consistent with MFE's decimated 8 Hz samples. We have reproduced in software the antialiasing filter and determined the best fit series at 54 Hz consistent with the known constraints in telemetry. Because the antialiasing filter is heavily biased to the past, this improved construction is more responsive to abrupt changes in the magnetic field. This technique suggests a new magnitude profile at higher resolution than the 8 Hz available in telemetry and also permits an estimate of the reconstruction error that shows up in Figure 2. These alternate reconstructions give some idea of the imprecision of the 8 Hz profiles and also the imprecision of the magnitudes of the reconstructed profile. For our considerations the ambiguity near the weakest fields is of the highest interest.

A2. Data Issues With Electric Field Determinations

[84] An overview of the electric field data collected between 0635 and 0715 UT on 29 May 1996 is presented in Figure A1. The first three panels give the full, three-dimensional, measured electric field in GSM coordinates. The bottom three panels give the same field computed by replacing the on-axis measurement with the assumption that this component of the electric field was zero. This assumption is utilized throughout the following discussion to compare fields produced with and without using the on-axis measurement in order to show that the less reliable, on-axis field measurement did not influence the parallel electric field results reported here. In particular, a stringent criterion for accepting a parallel electric field measurement will be that the parallel field does not depend on whether the measured on-axis component or the assumed zero value of the on-axis component was used in computing it.

[85] During times of data gaps in Figure A1 the preamplifiers of the electric field experiment on the Polar satellite oscillated because of positive feedback from the preamplifier outputs to the spherical sensors. Such intervals have been excluded from the electric field analyses discussed below.

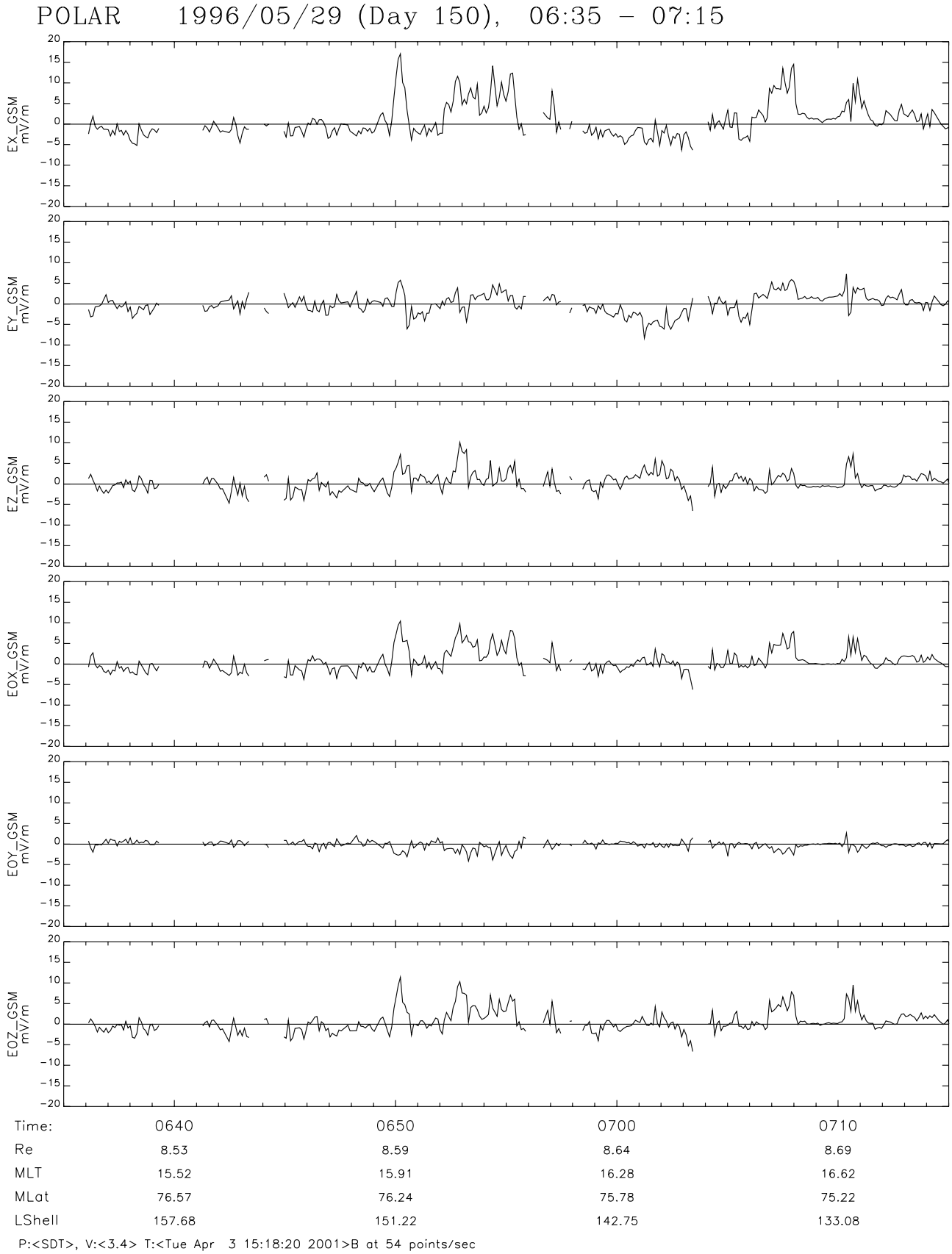

Figure A1. GSM electric field data 0635–0715 UT. First three panels depict all three components of **E** using all three EFI booms together. Last three panels depict all three components of a pseudo **E**, denoted by **E0**, where the on-axis boom measurements are not used, but $\mathbf{E} \cdot \mathbf{B} = 0$ is enforced.

[86] Many examples of parallel electric fields of a few mV m^{-1} were observed near the magnetopause crossings in this time interval (see magnetic field data in Figure 3). It is the purpose of this section to describe these parallel electric field observations after presenting evidence of the quality of the electric field measurement. This measurement is obtained from the potential differences between three pairs of spheres that are located at the ends of booms. Two of these sphere pairs are at the ends of wire booms that are extended and maintained in the spacecraft spin plane by centrifugal force. One pair is separated by 130 m (the output labeled V12), and the other pair is separated by 100 m (the output labeled V34). The third pair of spheres are aligned along the vehicle spin axis at a separation distance of 13.6 m (the output labeled V56). Instrument details are provided elsewhere [*Harvey et al.*, 1995].

[87] The first requirement for establishing the quality of the electric field measurement is to show that the pair of long wire booms in the spin plane produced good data at all densities. An example of this fact from the end of the time interval of interest when the density was $\sim$0.3 cm^{-3} is illustrated in Figure A2. The first two panels display electric fields obtained as the measured potential differences divided by the appropriate sphere separation distance. Each output varied with the 6 s Polar spin period due to the rotation of these spin-plane antennas in a quasi-static external field. The square root of the sum of the squares of these two measurements is presented in the third panel of Figure A2. There is no apparent 3 s, half-spin periodicity in the data of this third panel for fields as small as a fraction of a mV m^{-1}. In fact, the power at 0.33 Hz is 20 dB below the DC power, and no peak discernible in the noise at 0.33 Hz and >4 dB is observed. This is proof that the two independent detectors, whose lengths differed by 30%, measured the same electric field. The potential difference produced by an external electric field is proportional to the length of the antenna, so this potential difference divided by the separation distance (the quantity plotted in the first two panels) is the same for the two axes only if an external electric field was measured. A constant error signal measured by the two antennas would result in E12 being 30% smaller than E34, so the sixth panel of Figure A1 would vary in amplitude by 30% at the half-spin period. Also, a spacecraft perturbation of the electric field in its vicinity would be smaller at the spheres that are at the ends of the longer antennas. Such an error source would cause more than a 30% amplitude variation at the half-spin period. Thus the facts that E12 and E34 did not differ by 30% and that there was no half-spin periodicity in the total electric field in the spin plane are proof that the long wire antennas functioned properly in this environment. It is noted that small, DC offsets were subtracted from the data in the first two panels of Figure A2.

[88] Figure A3 presents similar data with a similar conclusion during an earlier segment of the interval when the plasma density was >30 cm^{-3} and the electric field fluctuations were typically faster than the spin period. Even so, there was not a 30% difference in the amplitudes of the two electric field outputs, and there was no apparent half-spin period oscillation in the third panel of this figure. In fact, the power at 0.33 Hz is 16 dB less than the DC power, and any peak at 0.33 Hz in the power spectrum is <3 dB. The time segment and data in this figure will be important in later discussions of parallel electric fields.

[89] The time interval of 0635–0715 UT has been searched manually for parallel electric fields, using only the electric field data and the magnetic field orientation (not the magnetic field magnitude or any plasma data). Thirteen intervals containing about a minute of data that satisfy the stringent criterion that the parallel electric field does not depend on whether it was determined by using the on-axis measurement or by assuming that the on-axis field component was zero have been found. This criterion probably causes some parallel electric field events to be missed and might cause short duration, high-density plasma events to be favored. Figure A4 presents the longest time interval during which parallel fields were found by the search criterion. The first three panels give the magnetic field in GSM coordinates. The magnetic field was depressed from its nominal $\sim$100 nT value because the spacecraft was in the vicinity of the separator, having moved from the magnetosheath magnetic field geometry ($Bx < 0$, $Bz > 0$) to that of the magnetosphere 4 s into the interval (This fact and the existence of the depressed magnetic field were not known or used while searching for this and other events). The electric field is presented in the last three panels of Figure A4 in a magnetic-field-aligned coordinate system in which the z axis is along the instantaneous magnetic field, the x axis points inward, perpendicular to the magnetic field and in the meridian plane, and the y axis is perpendicular to the magnetic field and in the generally westward direction. It is noted that the parallel electric field magnitude of a few mV m^{-1} is similar to the perpendicular field magnitude and that there is less of the higher-frequency turbulence in the parallel field than in the perpendicular field. There are several single point spikes in the field, and some of them (for example, near 0641:13.5 UT) have significant components in the parallel direction. These spikes are observed through the entire data set (see Figures A2 and A3).

[90] Evidence for the reality of the parallel electric field in Figure A4 is presented in Figure A5. The first panel of Figure A5 gives the spacecraft potential, which indicates that the plasma density did not vary significantly during this interval, so that offsets in the spin-axis electric field measurement are expected to be constant. The second panel is the measured parallel electric field that was also given in Figure A4. The fourth panel gives the direction cosine between the spin axis and the magnetic field. Because this direction cosine is often small in regions of nonzero parallel field, it is unlikely that such parallel fields come from offsets in the spin-axis measurement. If they did, the contribution of offsets to EY of Figure A4 would be typically three to five times bigger than their contribution to EZ, because the spin axis pointed mostly along the y-direction in the field-aligned coordinates. The final and best evidence for the reality of the measured parallel electric field is given by comparing the second and third panels of Figure A5, the latter of which, E0Z, is the parallel electric field that is determined by replacing the measured spin-axis component of the electric field by a zero value. For E0Z, all of the nonzero field is produced by measurements by the long wire boom pair. Because E0Z and EZ are essentially identical, an error in the spin-axis measurement could not have produced the measured parallel electric field.

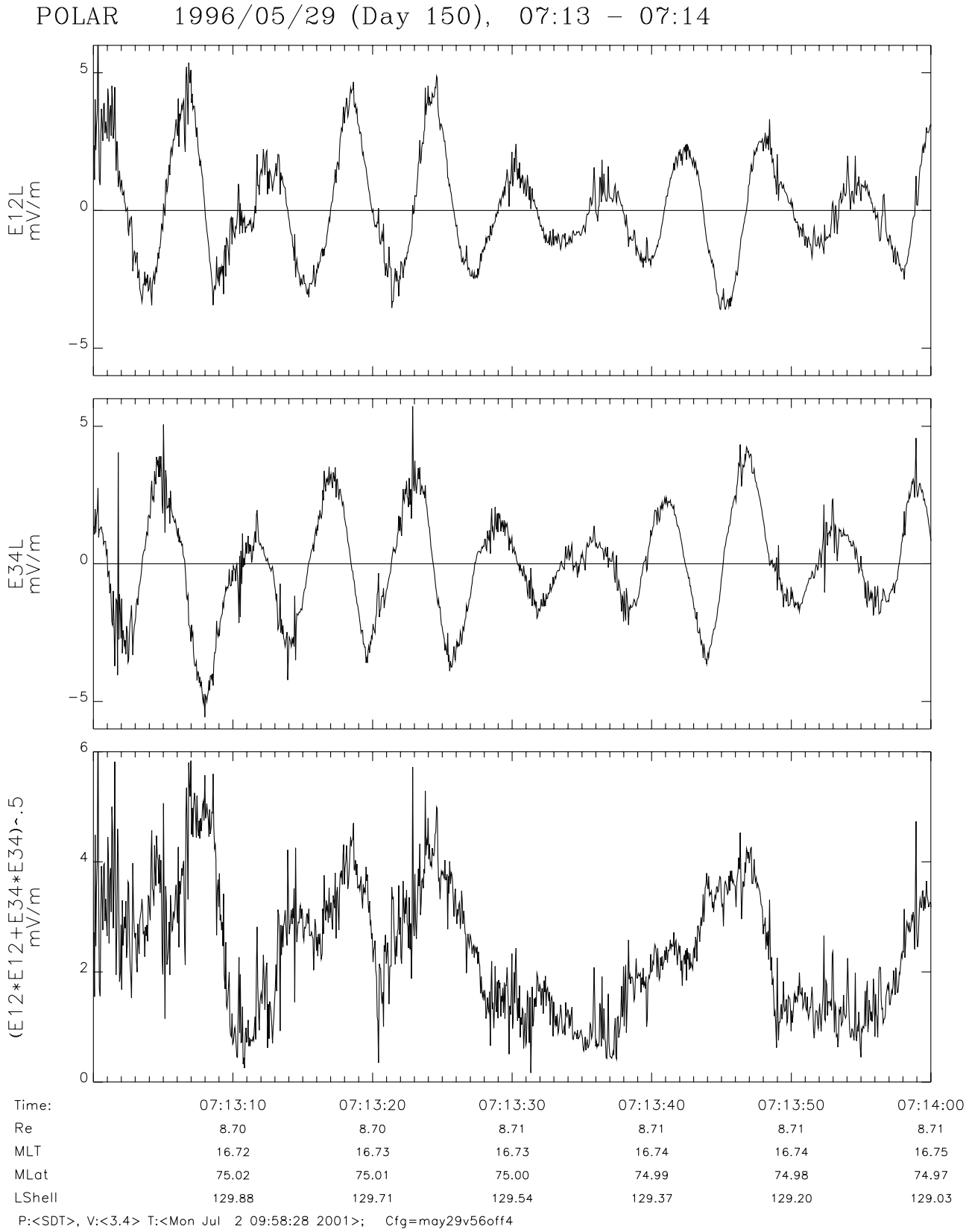

Figure A2. Electric field data in rotating sensor coordinates between 0713 and 0714 UT.

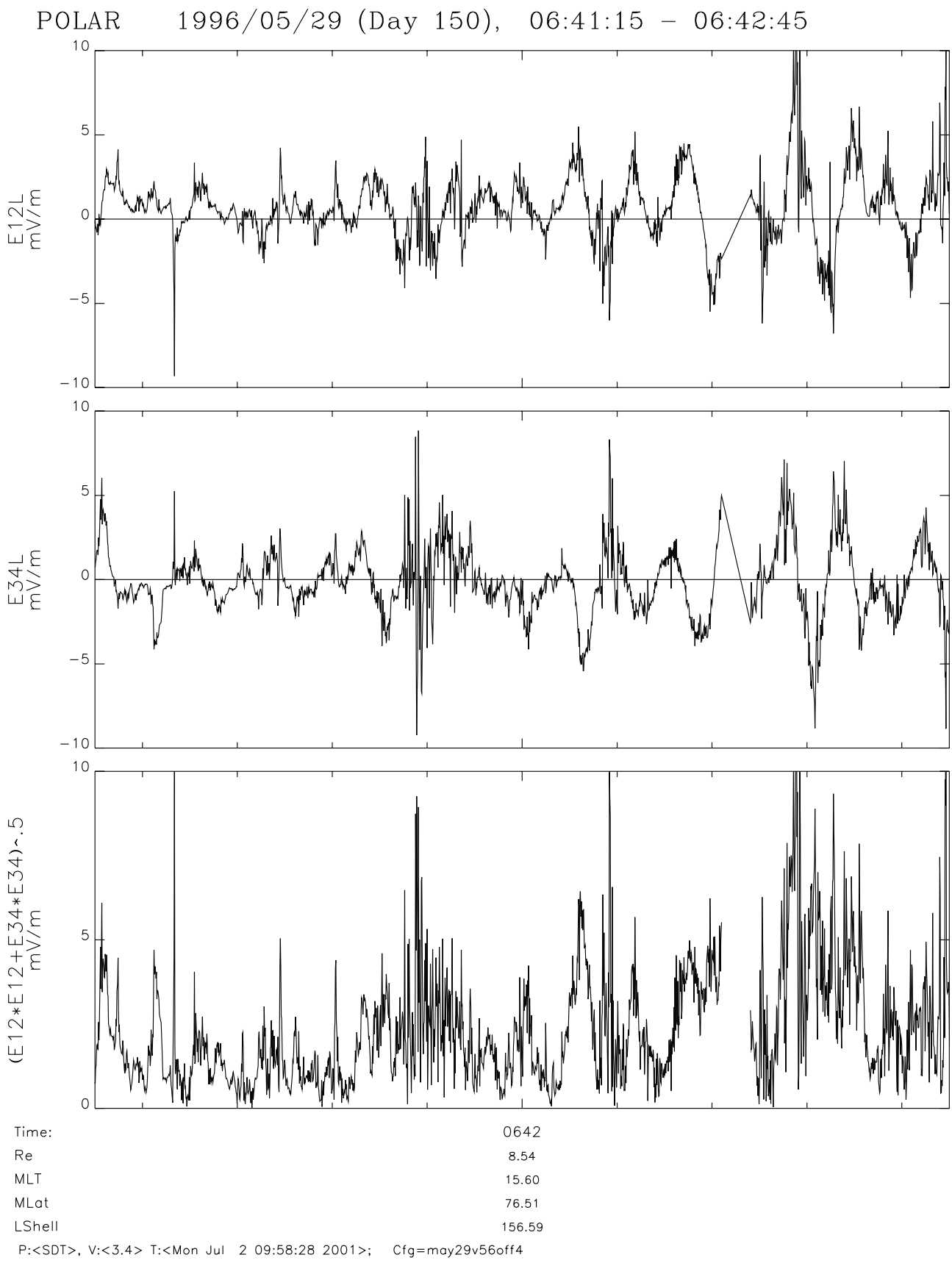

Figure A3. Electric field data in rotating sensor coordinates between 0713 and 0714 UT.

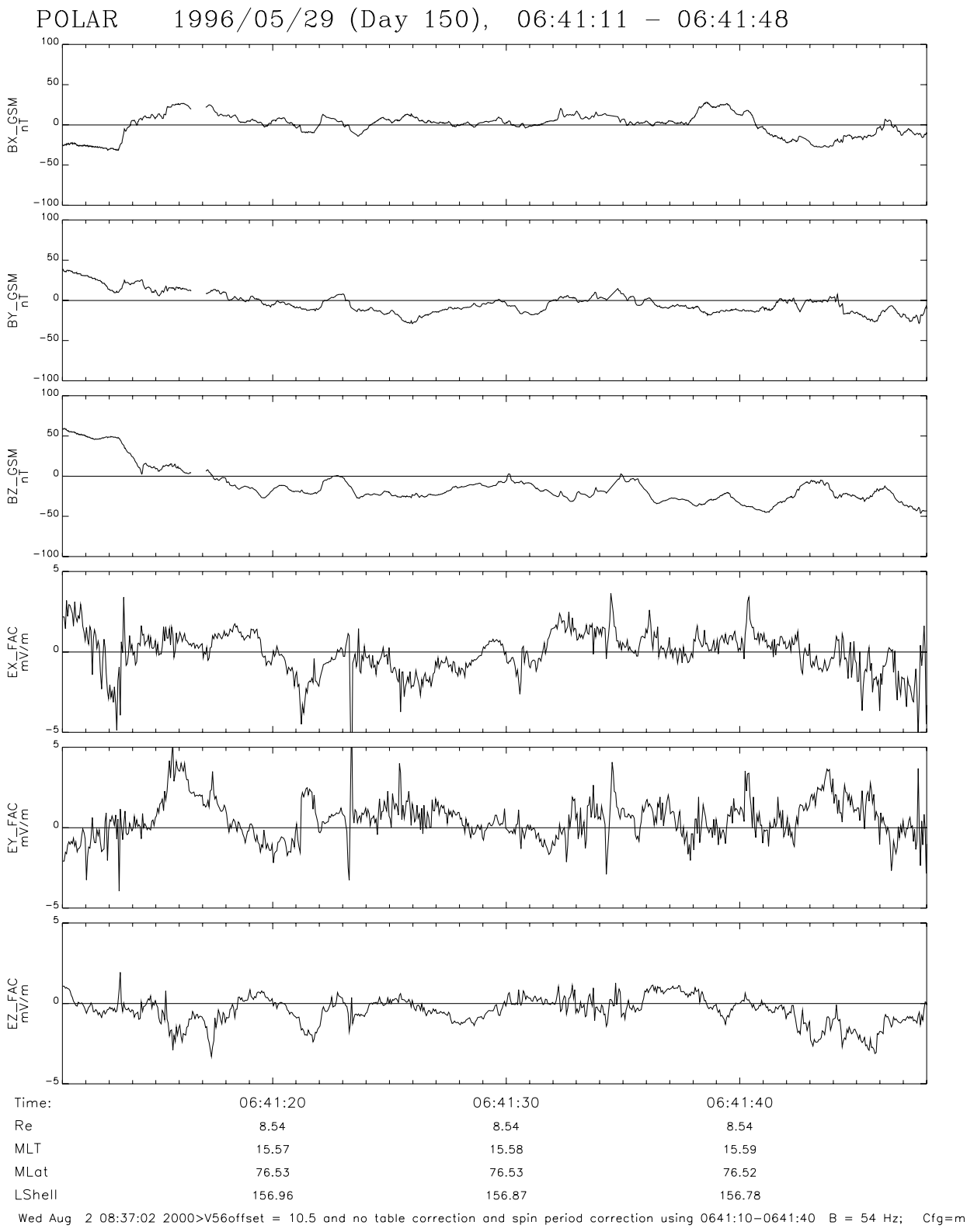

Figure A4. Electric and magnetic field data between 0641:11 and 0641:48 UT. The first three panels give the magnetic field components in GSM coordinates. The last three panels give the three components of the electric field, as determined from the full 3-axis measurement, in a magnetic field aligned coordinate system, $\mathbf{E}_i\mathbf{FAC}$. The *z*-component in the field-aligned coordinates is parallel to the locally measured magnetic field, the *x*-component is perpendicular to **B** and inward, and the *y*-component is perpendicular to **B** and points approximately westward. Note that the magnetic field is relatively small during this time interval, that the parallel electric field is nonzero, and that there is more turbulence in the perpendicular electric field than in the parallel electric field.

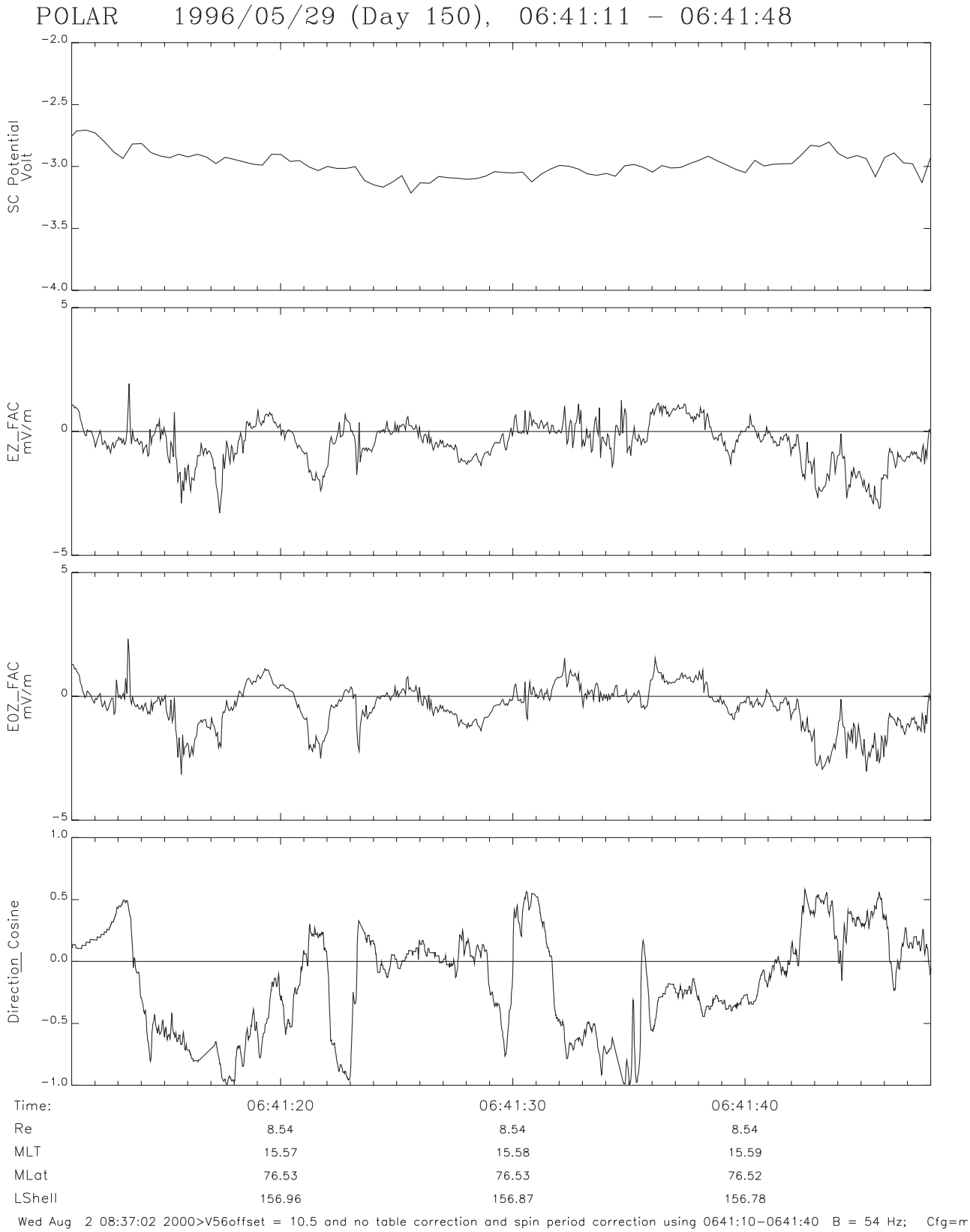

Figure A5. Field data obtained during the 37-s interval also described in Figure A4. The panels from top to bottom are the spacecraft potential, the parallel electric field produced from the full three component measurement, the parallel electric field produced from the spin plane measurements and the assumption that the on-axis component of electric field was zero, and the cosine of the angle between the on-axis boom and the magnetic field direction.

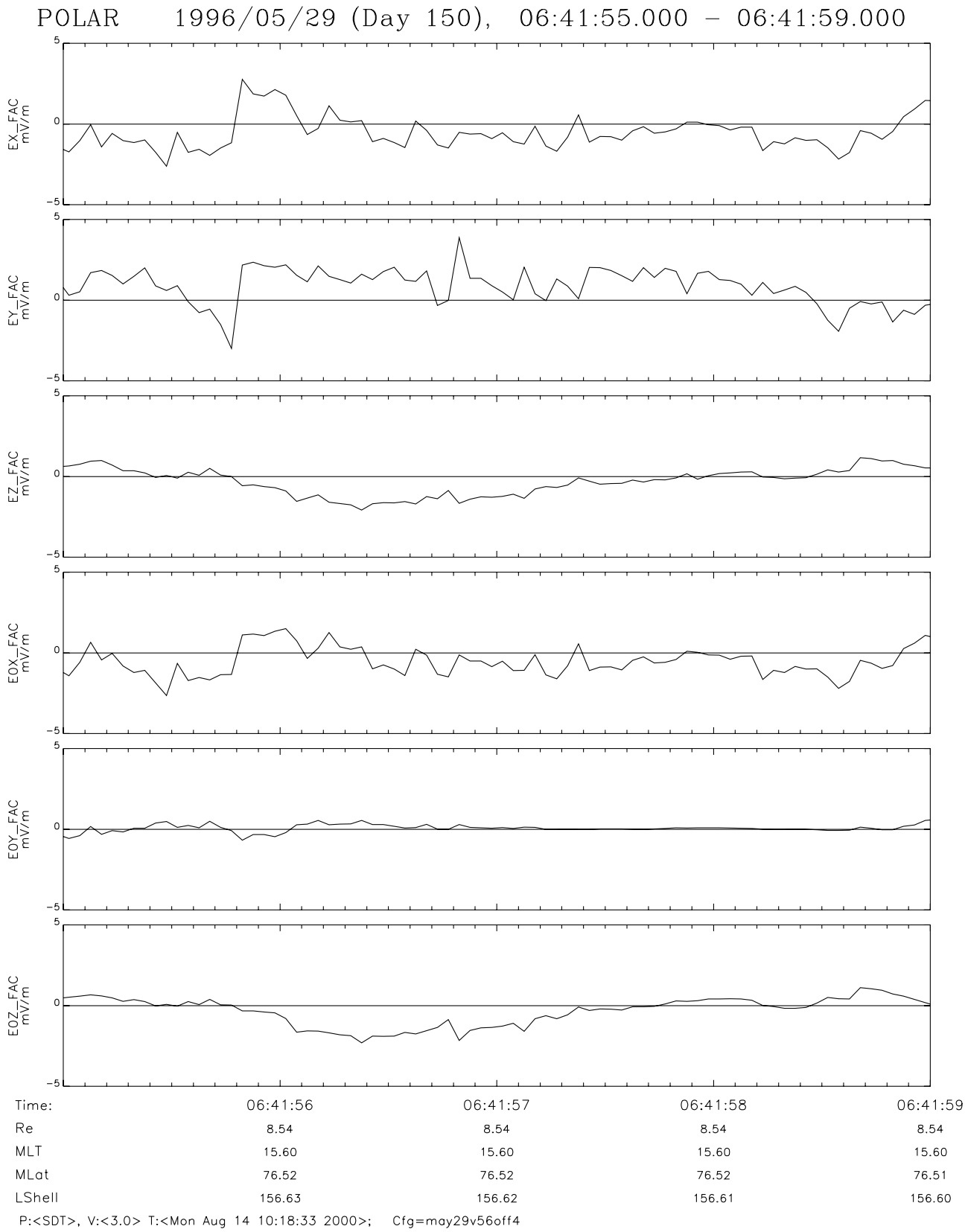

Figure A6. Electric field measurements in field-aligned coordinates from 0641:55 to 0641:59 UT. The first three panels give three components as determined from the full 3-axis measurement, and the last three panels give the three components obtained by replacing the spin-axis field measurement by the assumption that this component of the electric field was zero.

[91] Another example of a nonzero parallel electric field is illustrated in Figure A6, in which the first three panels are the components of the electric field in the field-aligned coordinate system and the last three panels are the same components computed by assuming that the spin-axis electric field was zero. Again, because EZ is essentially equal to E0Z, the parallel field did not result from measurements made by the spin-axis booms. This is because the magnetic field was nearly perpendicular to the spin axis, being within 10° of the spin plane for the entire time interval. In this orientation, magnetic-field-aligned wakes have sometimes caused perturbations of the electric field measurements made by sphere pairs that are on nearly the same magnetic field line as the spacecraft. That this did not happen in this example is shown by the lack of anomalies when either boom was most closely aligned with the magnetic field. Boom E12 was within 10° of the magnetic field line at 0641:56.1–0641:56.2 and 0641:58.3–0641:58.5 UT. Boom E34 was within 10° of the magnetic field line at 0641:55.6–0641:55.8 and 0641:57.2–0641:57.4 UT. At none of these times were there any unusual anomalies in the resulting field or in the raw data (see Figure A2, which contains the time interval under discussion and which also shows that there were no half-spin period variations in the magnitude of the electric field measured in the spin plane). Because the magnetic field was nearly in the vehicle spin plane, the long, wire booms measured EX and EZ in the field-aligned coordinate system (This may also be seen by the fact that the only effect of the spin-axis measurement is in the difference between EY and E0Y in Figure A6). Because EX and EZ had comparable magnitudes, explaining the data as a failure in the measurement would require a mechanism for rotating the measured electric field in the spin plane through an angle of ~45°. No such explanation has been envisioned.

[92] Further bolstering the interpretation that a parallel electric field of a few mV m^{-1} was measured in Figure A6 is the fact that the data occurred in the middle of a time interval in which the spacecraft passed from the magnetosphere ($BX > 0$, $BZ < 0$) to the magnetosheath ($BX < 0$, $BZ > 0$) and the magnetic field was relatively weak. Statistical properties of the entire data set are discussed in the main text to show that the parallel electric field measurements are in excellent agreement with expectations based on reconnection theories and simulations.

A3. Hydra Fluid Determinations

[93] Given the novelty of the electron flow velocity measurements in the magnetopause vicinity, we seek general corroboration that the electron flow velocity measurements are credible. A moment's reflection outlines the technical difficulties with such determinations: The electron flow energy associated with a bulk motion of 200 km s^{-1} at the magnetopause is ≃0.1 eV, while the thermal spread for electrons in the magnetosheath/cusp environs ranges from 20 to 100 eV. Components of the flow speeds slower than this do occur within this region. Two measures of the difficulty are the small absolute energy that the convection represents and followed in close degree by the smallness of the convection speed in units of the thermal speed, the thermal Mach number. If the ion and electron flow speeds are nearly the same, the ion flow energy is increased by 1836, while the temperature of the ions is not increased by such a wide factor; hence the energy of the ion flows is in the several hundreds of eV range, and the peak of the velocity distribution function is much clearer by ratios that approach the square root of the mass ratio. An additional complication is the variable spacecraft potential that has values that range in sunlight between 0.1 and 0.5 kT_e. These potentials affect the collected particle's energy and direction of arrival. Previously, studies have been performed for data acquisition dispersed in angle and energy appropriate to the geometry of Hydra's electrostatic analyzers [*Scudder et al.*, 1995, 1986, 1999] where it has been shown that the figure of precision to be anticipated per component for the electron flow velocity is approximately $\delta \simeq 25 \text{ km s}^{-1}\sqrt{\frac{T_e}{2\times10^5\text{K}}}$ indicated in Figures 10 and 11.

A3.1. Numerical Integrations of Moments

[94] The numerical integrations used by the Hydra team to determine the moments are discussed by *Scudder et al.* [1995]. In preparation for this study we have used the generalized Walén test [*Scudder et al.*, 1999] for the data of this day to ascertain the presence of rotational discontinuities. These tests involve the vectorial differences of electron flow velocities that are supposed to be strictly proportional to corresponding magnetic field changes. The unprecedented quality of those tests indicate that the vectorial precision of the electron flow velocities are high enough to provide the first quantitative verification of detection of rotational discontinuities within the magnetopause layer. The normalized χ^2_ν of these excellent fits also imply that the a priori error estimates of the electron flow speeds given above are consistently estimated.

A3.2. Subspin Period Fluid Quantities

[95] Fluid parameters for electrons at 4.6-s resolution have also been used in this paper. Extensive checks have been performed that vectorial quantities obtained at the higher time resolution do predict the lower time resolution numerical values of the moments. This check is almost perfect in all components of the electron bulk flow, for example, when the magnetic field direction is sufficiently stable during the data acquisition for the 13.8 s direct numerical integrated quantities.

A3.3. Spacecraft Potential Corrections and Ross Checks

[96] The EFI subsystem usually supplies in telemetry an estimate of the spacecraft floating potential that has been closely compared with its ability to delineate collected photoelectrons in the Hydra observations [*Scudder et al.*, 2000]. The systematic relationship of the value of this potential and the current density presented to the spacecraft by the plasma has been analyzed elsewhere [*Scudder et al.*, 2000] to the end that the spacecraft potential may be determined even when the EFI subsystem cannot supply it. We have also documented the precision with which the potential brings the ambient electron and ion density into agreement; data for the day of this cusp encounter have been examined with much care, and the systematics have been discussed in that publication.

A3.4. Hydra Detector Intercalibrations

[97] The determination of bulk moments of the ultrasubsonic electrons requires careful intracalibration of the various sensing elements whose fluxes are ultimately compared in the process of numerical integration to determine

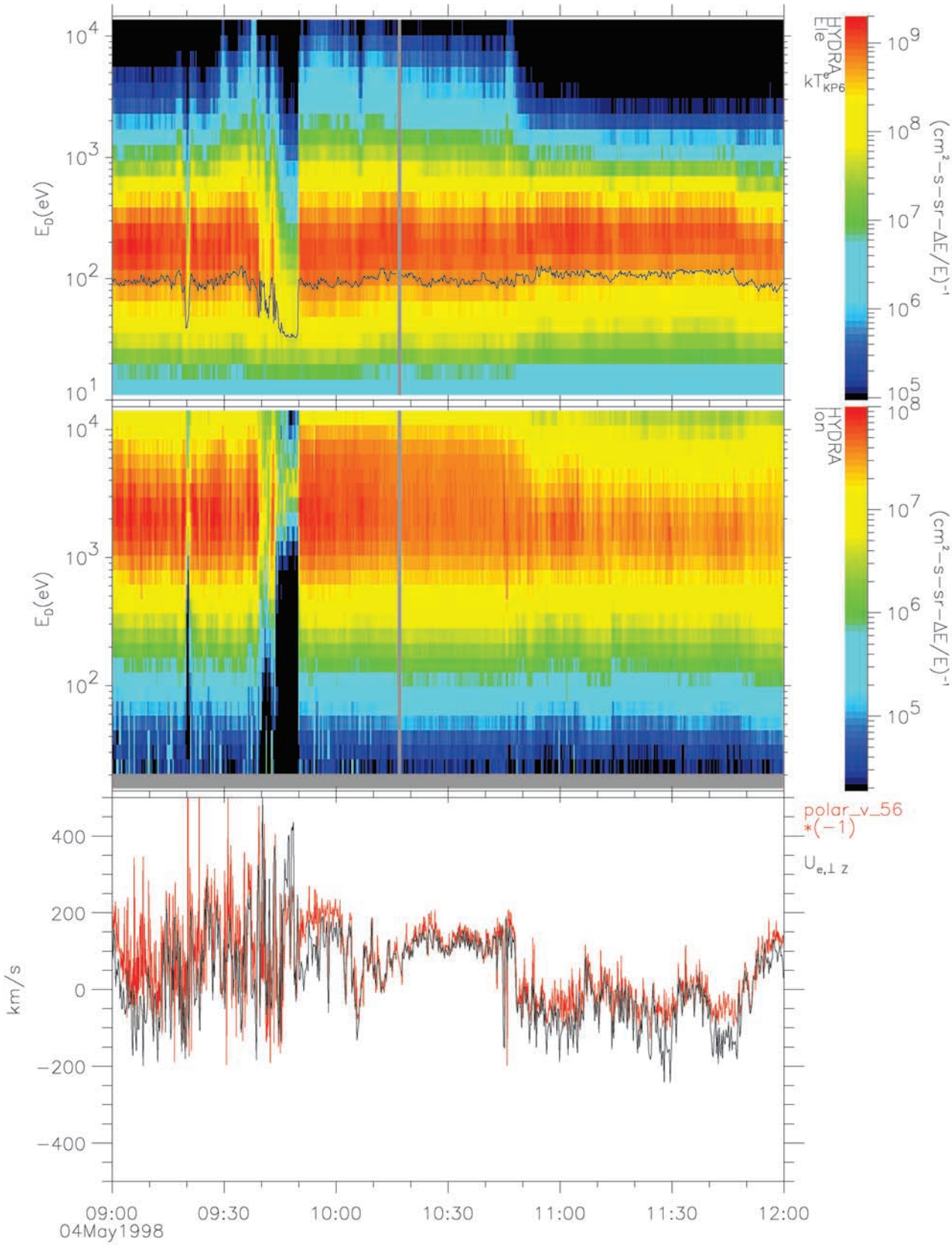

Figure A7. 4 May 1998 data in the deep magnetosheath with brief episodes in the solar wind. Electron and ion spectrograms (first two panels) and comparison of the spin axis component of the perpendicular component of the electron fluid velocity (black) and the z-component of $\mathbf{E} \times \mathbf{B}$. Mean energy of electron gas is indicated in the black overplotted trace in the first panel.

the bulk statistics. Hydra's twelve narrow field of view sensor heads have their own sensing elements and optics that are virtually identical, but not exactly so. The efficiency of the channeltrons requires ongoing intracalibration. Using 1-week blocks of Hydra data and the 54 Hz high resolution magnetic field directions, we look for circumstances when two detectors are looking at the same pitch angle, while sampling at the same energy. All such pairwise comparisons are used to cross-calibrate the twelve sensor heads as a least squares problem between two signals that have Poisson noise. This procedure is done weekly across intervals of constant channeltron-accelerating voltage, after the removal of sunlight and penetrating backgrounds and periods where the ions suggest flows are present. We have shown that these intracalibrations are consistent from week to week and are slowly varying on longer time scales. We use these variations or any sudden changes in them to assess the health of the instrument and to gauge the saturation of all the channeltrons.

A3.5. Data Products: $\mathbf{U}_{\perp,e}$ and $\mathbf{E} \times \mathbf{B}$ Comparisons

[98] We routinely cross-check the electron flow parameters by ascertaining their behavior relative to $\mathbf{E} \times \mathbf{B}$. In this section we illustrate in Figure A7 such a comparison on one of the relatively rare occasions when Polar punched out into the solar wind, giving a long passage through the magnetosheath.

[99] Two passages into the solar wind occur centered on 0914 and 0944–0947 UT. In the remainder of this interval, Polar is in the magnetosheath. From the electron spectrograms the spacecraft remains close to the shock 0928–1048 UT as indicated by the proximity of intense, multi-keV electron fluxes that are not typically part of the normal magnetosheath, seen after 1048 UT. The shocked gas, especially the electrons, is unusually hot, indicative of the high momentum flux of the solar wind at this time. The third panel of Figure A7 illustrates in an overplot format the electron fluid's bulk flow across the local magnetic field direction along the spin axis, $\mathbf{U}_{\perp,e} \cdot \hat{\mathbf{z}}$ (black, 13.8-s resolution), and the spin-axis component of $\mathbf{E} \times \mathbf{B}$ plotted first in (red, spin resolution). During this period, there is a change in this flow component of over 600 km s^{-1}, and as expected, the electron bulk index (Hydra) is tracking well the electric drift as independently determined from MFE and EFI data. At abrupt boundaries that are traversed more quickly than 6 s, the spin fit determinations and the Hydra numerical integrations are aliased differently (Such an effect can be seen near 1045:33 UT where a jagged red trace extends well below the black trace on the boundary in time where the high energy electrons are strongly encountered). There are other intervals near the entrances or exits to the shock transition where this effect may also be seen. On the whole the two diagnostics track one another rather well, even out into the solar wind. At 100 eV, typical of the interval beyond 1100 UT, the expected numerical uncertainty is 56 km s^{-1}, using the rule that generates the size of the δ quantities in Figures 11 and 12. The agreement between the electric drift and the cross-field electron drift is often better than this but is of this order in this demonstration. There are intervals behind the shock and in the pedestal region where pressure gradient effects such as are being discussed in this paper may be important, but on the whole, Figure A7 demonstrates the routine recovery of the electric drift in the magnetosheath proper where it is expected that these quantities should be essentially synonymous.

A3.6. Data Products: Quality Control

[100] Routine checks performed on the respective moment data for electrons and ions involve determining the numerical disparity of the charge density of the ions and electrons. This comparison is done in such a way to evaluate whether the computed differences are within the expected errors in the determination of the floating potential, electron temperature, and Poisson statistics. An example of such an analysis done for this day is illustrated by *Scudder et al.* [2000]. There are periods in the plasma sphere well away from the data of the event of this paper where this type of analysis clearly shows that there are disagreements between the ion and electron densities inferred from measurements within Hydra's energy range. These disagreements have been inverted using the spacecraft return current relationship and UHR density estimates to determine even the electron temperature through the plasma sphere. Routine checks are performed on the moment parameters by assessing the gyrotropy of the pressure tensor as determined in the drifting frame. If the plasma circumstances warrant a large-scale picture, it is expected that the departures from gyrotropy should be small and depend on counting statistics in the correct way. We also check that the principal axis of this tensor corresponding to the singular eigenvalue, a proxy magnetic field direction, agrees with the simultaneously averaged field direction transmitted in the MFE data stream. Unless the density is too low or the pressure anisotropy too small, this is generally a good vernier indicator of the success of the moment integration process, including correction for the effects of convection.

[101] **Acknowledgments.** The data from the three instruments in this paper are available as a result of a planning, fabrication, and data analysis process that spans over two decades of effort prior to this publication. The authors thank persons too numerous to list that have made this work possible. We also would like to salute the pivotal roles played by Stan Shawhan, Mario Acuña, and John Hrastar, who sustained the GGS and Polar Mission concept through its darkest hours. One of us (JS) acknowledges useful discussions and suggestions from A. Bhattacharjee and Z. Ma and commends the programming support provided by R. D. Holdaway and J. B. Faden, all at the University of Iowa. Work on the Hydra, EFI, and MFE data analysis is provided by NASA grants NAG 5-7883, 5-3182, and 5-7721 to the University of Iowa, the University of California at Berkeley, and the University of California at Los Angeles, respectively. We appreciate the referees' and guest editor's comments on the manuscript.

[102] S. Peter Gary thanks Goetz Paschmann and Joachim Birn for their assistance in evaluating this paper.

References

Aubry, M. P., M. G. Kivelson, and C. T. Russell, Motion and structure of the magnetopause, *J. Geophys. Res.*, *76*, 1673–1696, 1971.

Chandler, M. O., S. A. Fuselier, M. Lockwood, and T. E. Moore, Evidence of component merging equatorward of the cusp, *J. Geophys. Res.*, *104*, 22,623–22,634, 1999.

Cowley, S. W. H., Plasma populations in a simple open magnetosphere, *Space Sci. Rev.*, *26*, 217–275, 1980.

Crooker, N. U., Dayside merging and cusp geometry, *J. Geophys. Res.*, *84*, 951–959, 1979.

Dunlop, M., A. Balogh, W. Baumjohann, G. Haerendel, K.-H. Fornacon, E. Georgescu, R. Nakamura, and S. Kokubin, Dynamics and local boundary properties of the dawnside magnetopause under conditions observed by Equator-S, *Ann. Geophys.*, *17*, 1535–1559, 1999.

Farrugia, C. J., et al., Geoeffectiveness of three Wind magnetic clouds: A comparative study, *J. Geophys. Res.*, *103*, 17,261–17,278, 1998.

Fuselier, S. A., K. J. Trattner, and S. M. Petrinec, Cusp observations of

high- and low-latitude reconnection for northward interplanetary magnetic field, *J. Geophys. Res.*, *105*, 253–266, 2000.
Gosling, J. T., M. F. Thomsen, S. J. Bame, R. C. Elphic, and C. T. Russell, Plasma flow reversals at the dayside magnetopause and the origin of asymmetric polar cap convection, *J. Geophys. Res.*, *95*, 8073–8084, 1990.
Gosling, J. T., M. F. Thomsen, S. J. Bame, and C. T. Russell, Accelerated plasma flows at the near-tail magnetopause, *J. Geophys. Res.*, *91*, 3029–3041, 1986.
Grande, M., J. Fennell, S. Livi, B. Kellett, C. Perry, P. Anderson, J. Roeder, H. Spence, T. Fritz, and B. Wilken, et al., First polar and 1995-034 observations of the midaltitude cusp during a persistent northward IMF condition, *Geophys. Res. Lett.*, *24*, 1475–1478, 1997.
Greene, J. M., Geometrical properties of three-dimensional reconnecting magnetic fields with nulls, *J. Geophys. Res.*, *93*, 8583–8590, 1988.
Harvey, P., et al., The electric field instrument on the polar spacecraft, in *The Global Geospace Mission*, edited by C. Russell, pp. 583–596, Kluwer Acad., Norwell, Mass., 1995.
Hesse, M., and K. Schindler, A theoretical foundation of general magnetic reconnection, *J. Geophys. Res.*, *93*, 5559–5567, 1988.
Hesse, M., D. Winske, and M. Kuznetsova, Hybrid modeling of collisionless reconnection in two-dimensional current sheets: Simulations, *J. Geophys. Res.*, *100*, 21,815–21,826, 1995.
Hesse, M., J. Birn, and M. Kuznetsova, Collisionless magnetic reconnection: Electron processes and transport modeling, *J. Geophys. Res.*, *106*, 3721–3735, 2001.
Ma, Z. W., and A. Bhattacharjee, Fast impulsive reconnection and current sheet intensification due to electron pressure gradients in semicollisional plasmas, *Geophys. Res. Lett.*, *23*, 1673–1676, 1996.
Mandt, M. E., R. E. Denton, and J. F. Drake, Transition to whistler mediated reconnection, *Geophys. Res. Lett.*, *21*, 73–75, 1994.
Neugebauer, M., C. T. Russell, and E. J. Smith, Observations of the internal structure of the magnetopause, *J. Geophys. Res.*, *79*, 499–510, 1974.
Oieroset, M., T. Phan, M. Fujimoto, R. Lin, and R. Lepping, In situ detection of collisionless reconnection in the Earth's magnetotail, *Nature*, *412*, 414–417, 2001.
Onsager, T., and M. Lockwood, High-latitude particle precipitation and its relationship to magnetospheric source regions, *Space Sci. Rev*, *80*, 77–107, 1997.
Onsager, T., J. D. Scudder, M. Lockwood, and C. Russell, Reconnection at the high-latitude magnetopause during the northward interplanetary magnetic field conditions, *J. Geophys. Res.*, *106*, 25,467–25,488, 2001.
Pannekoek, A., Ionization in stellar atmospheres, *Bull. Astron. Inst. Neth.*, *1*, 107–118, 1922.
Paschmann, G., Observational evidence for transfer of plasma across the magnetopause, *Space Sci. Rev*, *80*, 217–234, 1997.
Paschmann, G., I. Papamastorakis, W. Baumjohann, N. Sckopke, C. W. Carlson, B. U. Ö. Sonnerup, and H. Luhr, The magnetopause for large magnetic shear: AMPTE/IRM observations, *J. Geophys. Res.*, *91*, 11,099–11,115, 1986.
Press, W., S. Teukolsky, W. Vetterling, and B. Flannery, *Numerical Recipes*, Cambridge Univ. Press, New York, 1996.
Pritchett, P. L., Geospace environment modeling magnetic reconnection challenge: Simulations with a full particle electromagnetic code, *J. Geophys. Res.*, *106*, 3783–3798, 2001.
Pritchett, P. L., F. V. Coroniti, R. Pellat, and H. Karimabadi, Collisionless reconnection in two-dimensional magnetotail equilibria, *J. Geophys. Res.*, *96*, 11,523–11,538, 1991.
Rosseland, S., Electrical state of a star, *Mon. Not. R. Astron. Soc.*, *84*, 720–728, 1924.
Rossi, B., and S. Olbert, *Introduction to the Physics of Space*, McGraw-Hill, New York, 1970.
Russell, C. T., R. Snare, J. D. Means, D. Pierce, D. Dearborn, M. Larson, G. Barr, and G. Le, The GGS/Polar magnetic fields investigation, in *The Global Geospace Mission*, pp. 563–582, Kluwer Acad., Norwell, Mass., 1995.
Russell, C. T., J. A. Fedder, S. P. Slinker, X.-W. Zhou, G. Le, J. G. Luhmann, F. R. Fenrich, M. O. Chandler, T. E. Moore, and S. A. Fuselier, Entry of the POLAR spacecraft into the polar cusp under northward IMF conditions., *Geophys. Res. Lett.*, *25*, 3015–3018, 1998.
Savin, S. P., et al., The cusp/magnetosheath interface on May 29, 1996: Interball-1 and Polar observations, *Geophys. Res. Lett.*, *25*, 2963–2966, 1998.
Schindler, K., M. Hesse, and J. Birn, General magnetic reconnection, parallel electric fields, and helicity, *J. Geophys. Res.*, *93*, 5547–5557, 1988.
Scudder, J. D., Theoretical approaches to the description of magnetic merging: The need for finite β_e, anisotropic ambipolar Hall MHD, *Space Sci. Rev.*, *80*, 235–267, 1997.
Scudder, J. D., K. W. Ogilvie, and C. Russell, The relationship of flux transfer events to magnetic reconnection, in *Magnetic Reconnection in Space and Laboratory Plasmas*, *Geophys. Monogr. Ser.*, vol. 30, edited by E. W. Hones, pp. 153–154, AGU, Washington, D. C., 1984.
Scudder, J. D., A. Mangeney, C. Lacombe, C. C. Harvey, T. L. Aggson, R. R. Anderson, J. T. Gosling, G. Paschmann, and C. T. Russell, The resolved layer of a collisionless, high β, supercritical, quasi-perpendicular shock wave, 1, Rankine-Hugoniot geometry, currents and stationarity, *J. Geophys. Res.*, *91*, 11,019–11,052, 1986.
Scudder, J. D., et al., Hydra-A 3-dimensional electron and ion hot plasma instrument for the Polar spacecraft of the GGS mission, in *The Global Geospace Mission*, edited by C. T. Russell, pp. 459–495, Kluwer Acad., Norwell, Mass., 1995.
Scudder, J. D., P. Puhl-Quinn, F. S. Mozer, C. T. Russell, and K. Ogilvie, Generalized Walén tests through Alfvén waves and rotational discontinuities using electron flow velocities, *J. Geophys. Res.*, *104*, 19,817–19,833, 1999.
Scudder, J. D., X. Cao, and F. Mozer, The photoemission current-spacecraft voltage relation: Key to routine, quantitative low-energy plasma measurements, *J. Geophys. Res.*, *105*, 21,281–21,294, 2000.
Shay, M. A., J. F. Drake, R. E. Denton, and D. Biskamp, Structure of the dissipation region during collisionless magnetic reconnection, *J. Geophys. Res.*, *103*, 9165–9176, 1998.
Shay, M. A., J. F. Drake, B. N. Rogers, and R. E. Denton, Alfvénic collisionless magnetic reconnection and the Hall term, *J. Geophys. Res.*, *106*, 3759–3772, 2001.
Siscoe, G., The magnetospheric boundary, in *Physics of Space Plasmas*, edited by T. Chang, G. B. Crew, and J. R. Jasperse, pp. 3–78, Scientific, Gainesville, Fla., 1988.
Sonnerup, B. U. Ö., Magnetic field reconnection, in *Solar System Plasma Physics*, edited by E. N. Parker, C. F. Kennel, and L. J. Lanzerotti, pp. 45–108, North-Holland, New York, 1979.
Sonnerup, B. U. Ö., On the theory of steady state reconnection, *Comput. Phys. Commun.*, *49*, 143–159, 1988.
Sonnerup, B. U. Ö., and L. Cahill, Explorer 12 observations of the magnetopause current layer, *J. Geophys. Res.*, *73*, 1757–1770, 1968.
Sonnerup, B. U. Ö., G. Paschmann, I. Papamastorakis, N. Sckopke, G. Haerendel, S. J. Bame, J. R. Asbridge, J. T. Gosling, and C. T. Russell, Evidence for magnetic field reconnection at the Earth's magnetopause, *J. Geophys. Res.*, *86*, 10,049–10,067, 1981.
Sonnerup, B. U. Ö., G. Paschmann, and T. D. Phan, Fluid aspects of reconnection at the magnetopause: In situ observations, in *Physics of the Magnetopause*, *Geophys. Monogr. Ser.*, vol. 90, edited by P. Song, B. U. Ö. Sonnerup, and M. F. Thomsen, pp. 167–180, AGU, Washington, D. C., 1995.
Stern, D. P., A study of the electric field in an open magnetospheric model, *J. Geophys. Res.*, *78*, 7292–7305, 1973.
Urquhart, A. L., P. H. Reiff, F. R. Toffoletto, T. W. Hill, T. R. Konkel, C. T. Russell, G. Le, S. P. Savin, and S. A. Romanov, Polar magnetopause crossings of May 29, 1996: Implications for magnetic modeling, *J. Geophys. Res.*, *103*, 17,323–17,332, 1998.
Vasyliunas, V. M., Theoretical models of magnetic field line merging, 1, *Rev. Geophys.*, *13*, 303–336, 1975.
Vasyliunas, V., Steady state aspects of magnetic field line merging, in *Magnetic Reconnection in Space and Laboratory Plasmas*, *Geophys. Monogr. Ser.*, vol. 30, edited by E. W. Hones, pp. 25–31, AGU, Washington, D. C., 1984.
Vasyliunas, V., Large-scales of the ionosphere/magnetosphere/solar wind system-MHD as a unifying principle, in *Modeling Magnetospheric Plasma*, *Geophys. Monogr. Ser.*, vol. 44, edited by T. E. Moore and J. H. Waite Jr., pp. 33–37, AGU, Washington, D. C., 1988.
Zakharov, L., and B. Rogers, Two fluid magnetohydrodynamic descriptions of the internal kink mode in tokamaks, *Phys. Fluids B*, *4*, 3285–3301, 1992.

N. C. Maynard, Mission Research Corporation, 589 West Holly Street, Suite 201, Nashua, NH 03062, USA. (nmaynard@mrcnh.com)
F. S. Mozer, Space Sciences Laboratory, University of California, Berkeley, Berkeley, CA 94720, USA. (mozer@sunspot.ssl.berkeley.edu)
C. T. Russell, Institute of Geophysics and Planetary Physics, University of California, Los Angeles, 3845 Slichter Hall, 405 Hilgard Avenue, Los Angeles, CA 90095, USA. (ctrussel@igpp.ucla.edu)
J. D. Scudder, Department of Physics and Astronomy, University of Iowa, Iowa City, IA 52242, USA. (jds@space-theory.physics.uiowa.edu)